

A STUDY OF THE ORIENTATION AND ENERGY PARTITION OF THREE-JET EVENTS IN HADRONIC Z^0 DECAYS*

The SLD Collaboration[◇]

Stanford Linear Accelerator Center, Stanford University,
Stanford, CA 94309

Submitted to *Physical Review D*

*Work supported by U.S. Department of Energy contracts: DE-FG02-91ER40676 (BU), DE-FG03-92ER40701 (CIT), DE-FG03-91ER40618 (UCSB), DE-FG03-92ER40689 (UCSC), DE-FG03-93ER40788 (CSU), DE-FG02-91ER40672 (Colorado), DE-FG02-91ER40677 (Illinois), DE-AC03-76SF00098 (LBL), DE-FG02-92ER40715 (Massachusetts), DE-AC02-76ER03069 (MIT), DE-FG06-85ER40224 (Oregon), DE-AC03-76SF00515 (SLAC), DE-FG05-91ER40627 (Tennessee), DE-AC02-76ER00881 (Wisconsin), DE-FG02-92ER40704 (Yale); U.S. National Science Foundation grants: PHY-91-13428 (UCSC), PHY-89-21320 (Columbia), PHY-92-04239 (Cincinnati), PHY-88-17930 (Rutgers), PHY-88-19316 (Vanderbilt), PHY-92-03212 (Washington); the UK Science and Engineering Research Council (Brunel and RAL); the Istituto Nazionale di Fisica Nucleare of Italy (Bologna, Ferrara, Frascati, Pisa, Padova, Perugia); and the Japan-US Cooperative Research Project on High Energy Physics (Nagoya, Tohoku).

◇ K. Abe,⁽²⁰⁾ K. Abe,⁽³⁰⁾ I. Abt,⁽¹⁴⁾ T. Akagi,⁽²⁸⁾ N.J. Allen,⁽⁴⁾ W.W. Ash,^{(28)†}
 D. Aston,⁽²⁸⁾ K.G. Baird,⁽²⁵⁾ C. Baltay,⁽³⁴⁾ H.R. Band,⁽³³⁾ M.B. Barakat,⁽³⁴⁾
 G. Baranko,⁽¹⁰⁾ O. Bardon,⁽¹⁶⁾ T. Barklow,⁽²⁸⁾ G.L. Bashindzhagyan,⁽¹⁹⁾ A.O. Bazarko,⁽¹¹⁾
 R. Ben-David,⁽³⁴⁾ A.C. Benvenuti,⁽²⁾ G.M. Bilei,⁽²³⁾ D. Bisello,⁽²²⁾ G. Blaylock,⁽⁷⁾
 J.R. Bogart,⁽²⁸⁾ T. Bolton,⁽¹¹⁾ G.R. Bower,⁽²⁸⁾ J.E. Brau,⁽²¹⁾ M. Breidenbach,⁽²⁸⁾
 W.M. Bugg,⁽²⁹⁾ D. Burke,⁽²⁸⁾ T.H. Burnett,⁽³²⁾ P.N. Burrows,⁽¹⁶⁾ W. Busza,⁽¹⁶⁾
 A. Calcaterra,⁽¹³⁾ D.O. Caldwell,⁽⁶⁾ D. Calloway,⁽²⁸⁾ B. Camanzi,⁽¹²⁾ M. Carpinelli,⁽²⁴⁾
 R. Cassell,⁽²⁸⁾ R. Castaldi,^{(24)(a)} A. Castro,⁽²²⁾ M. Cavalli-Sforza,⁽⁷⁾ A. Chou,⁽²⁸⁾
 E. Church,⁽³²⁾ H.O. Cohn,⁽²⁹⁾ J.A. Coller,⁽³⁾ V. Cook,⁽³²⁾ R. Cotton,⁽⁴⁾ R.F. Cowan,⁽¹⁶⁾
 D.G. Coyne,⁽⁷⁾ G. Crawford,⁽²⁸⁾ A. D'Oliveira,⁽⁸⁾ C.J.S. Damerell,⁽²⁶⁾ M. Daoudi,⁽²⁸⁾
 R. De Sangro,⁽¹³⁾ P. De Simone,⁽¹³⁾ R. Dell'Orso,⁽²⁴⁾ P.J. Dervan,⁽⁴⁾ M. Dima,⁽⁹⁾
 D.N. Dong,⁽¹⁶⁾ P.Y.C. Du,⁽²⁹⁾ R. Dubois,⁽²⁸⁾ B.I. Eisenstein,⁽¹⁴⁾ R. Elia,⁽²⁸⁾ E. Etzion,⁽⁴⁾
 D. Falciari,⁽²³⁾ C. Fan,⁽¹⁰⁾ M.J. Fero,⁽¹⁶⁾ R. Frey,⁽²¹⁾ K. Furuno,⁽²¹⁾ T. Gillman,⁽²⁶⁾
 G. Gladding,⁽¹⁴⁾ S. Gonzalez,⁽¹⁶⁾ G.D. Hallewell,⁽²⁸⁾ E.L. Hart,⁽²⁹⁾ A. Hasan,⁽⁴⁾
 Y. Hasegawa,⁽³⁰⁾ K. Hasuko,⁽³⁰⁾ S. Hedges,⁽³⁾ S.S. Hertzbach,⁽¹⁷⁾ M.D. Hildreth,⁽²⁸⁾
 J. Huber,⁽²¹⁾ M.E. Huffer,⁽²⁸⁾ E.W. Hughes,⁽²⁸⁾ H. Hwang,⁽²¹⁾ Y. Iwasaki,⁽³⁰⁾
 D.J. Jackson,⁽²⁶⁾ P. Jacques,⁽²⁵⁾ J. Jaros,⁽²⁸⁾ A.S. Johnson,⁽³⁾ J.R. Johnson,⁽³³⁾
 R.A. Johnson,⁽⁸⁾ T. Junk,⁽²⁸⁾ R. Kajikawa,⁽²⁰⁾ M. Kalelkar,⁽²⁵⁾ H. J. Kang,⁽²⁷⁾
 I. Karliner,⁽¹⁴⁾ H. Kawahara,⁽²⁸⁾ H.W. Kendall,⁽¹⁶⁾ Y. Kim,⁽²⁷⁾ M.E. King,⁽²⁸⁾ R. King,⁽²⁸⁾
 R.R. Kofler,⁽¹⁷⁾ N.M. Krishna,⁽¹⁰⁾ R.S. Kroeger,⁽¹⁸⁾ J.F. Labs,⁽²⁸⁾ M. Langston,⁽²¹⁾
 A. Lath,⁽¹⁶⁾ J.A. Lauber,⁽¹⁰⁾ D.W.G.S. Leith,⁽²⁸⁾ V. Lia,⁽¹⁶⁾ M.X. Liu,⁽³⁴⁾ X. Liu,⁽⁷⁾
 M. Loreti,⁽²²⁾ A. Lu,⁽⁶⁾ H.L. Lynch,⁽²⁸⁾ J. Ma,⁽³²⁾ G. Mancinelli,⁽²³⁾ S. Manly,⁽³⁴⁾
 G. Mantovani,⁽²³⁾ T.W. Markiewicz,⁽²⁸⁾ T. Maruyama,⁽²⁸⁾ R. Massetti,⁽²³⁾ H. Masuda,⁽²⁸⁾
 E. Mazzucato,⁽¹²⁾ A.K. McKemey,⁽⁴⁾ B.T. Meadows,⁽⁸⁾ R. Messner,⁽²⁸⁾ P.M. Mockett,⁽³²⁾
 K.C. Moffeit,⁽²⁸⁾ B. Mours,⁽²⁸⁾ D. Muller,⁽²⁸⁾ T. Nagamine,⁽²⁸⁾ S. Narita,⁽³⁰⁾
 U. Nauenberg,⁽¹⁰⁾ H. Neal,⁽²⁸⁾ M. Nussbaum,⁽⁸⁾ Y. Ohnishi,⁽²⁰⁾ L.S. Osborne,⁽¹⁶⁾
 R.S. Panvini,⁽³¹⁾ H. Park,⁽²¹⁾ T.J. Pavel,⁽²⁸⁾ I. Peruzzi,^{(13)(b)} M. Piccolo,⁽¹³⁾
 L. Piemontese,⁽¹²⁾ E. Pieroni,⁽²⁴⁾ K.T. Pitts,⁽²¹⁾ R.J. Plano,⁽²⁵⁾ R. Prepost,⁽³³⁾
 C.Y. Prescott,⁽²⁸⁾ G.D. Punkar,⁽²⁸⁾ J. Quigley,⁽¹⁶⁾ B.N. Ratcliff,⁽²⁸⁾ T.W. Reeves,⁽³¹⁾
 J. Reidy,⁽¹⁸⁾ P.E. Rensing,⁽²⁸⁾ T.G. Rizzo,⁽²⁸⁾ L.S. Rochester,⁽²⁸⁾ P.C. Rowson,⁽¹¹⁾
 J.J. Russell,⁽²⁸⁾ O.H. Saxton,⁽²⁸⁾ T. Schalk,⁽⁷⁾ R.H. Schindler,⁽²⁸⁾ B.A. Schumm,⁽¹⁵⁾
 S. Sen,⁽³⁴⁾ V.V. Serbo,⁽³³⁾ M.H. Shaevitz,⁽¹¹⁾ J.T. Shank,⁽³⁾ G. Shapiro,⁽¹⁵⁾
 D.J. Sherden,⁽²⁸⁾ K.D. Shmakov,⁽²⁹⁾ C. Simopoulos,⁽²⁸⁾ N.B. Sinev,⁽²¹⁾ S.R. Smith,⁽²⁸⁾
 J.A. Snyder,⁽³⁴⁾ P. Stamer,⁽²⁵⁾ H. Steiner,⁽¹⁵⁾ R. Steiner,⁽¹⁾ M.G. Strauss,⁽¹⁷⁾ D. Su,⁽²⁸⁾
 F. Suekane,⁽³⁰⁾ A. Sugiyama,⁽²⁰⁾ S. Suzuki,⁽²⁰⁾ M. Swartz,⁽²⁸⁾ A. Szumilo,⁽³²⁾
 T. Takahashi,⁽²⁸⁾ F.E. Taylor,⁽¹⁶⁾ E. Torrence,⁽¹⁶⁾ A.I. Trandafir,⁽¹⁷⁾ J.D. Turk,⁽³⁴⁾
 T. Usher,⁽²⁸⁾ J. Va'vra,⁽²⁸⁾ C. Vannini,⁽²⁴⁾ E. Vella,⁽²⁸⁾ J.P. Venuti,⁽³¹⁾ R. Verdier,⁽¹⁶⁾
 P.G. Verdini,⁽²⁴⁾ S.R. Wagner,⁽²⁸⁾ A.P. Waite,⁽²⁸⁾ S.J. Watts,⁽⁴⁾ A.W. Weidemann,⁽²⁹⁾
 E.R. Weiss,⁽³²⁾ J.S. Whitaker,⁽³⁾ S.L. White,⁽²⁹⁾ F.J. Wickens,⁽²⁶⁾ D.A. Williams,⁽⁷⁾
 D.C. Williams,⁽¹⁶⁾ S.H. Williams,⁽²⁸⁾ S. Willocq,⁽³⁴⁾ R.J. Wilson,⁽⁹⁾ W.J. Wisniewski,⁽²⁸⁾
 M. Woods,⁽²⁸⁾ G.B. Word,⁽²⁵⁾ J. Wyss,⁽²²⁾ R.K. Yamamoto,⁽¹⁶⁾ J.M. Yamartino,⁽¹⁶⁾
 X. Yang,⁽²¹⁾ S.J. Yellin,⁽⁶⁾ C.C. Young,⁽²⁸⁾ H. Yuta,⁽³⁰⁾ G. Zapalac,⁽³³⁾ R.W. Zdarko,⁽²⁸⁾
 C. Zeitlin,⁽²¹⁾ and J. Zhou,⁽²¹⁾

- (¹) *Adelphi University, Garden City, New York 11530*
 (²) *INFN Sezione di Bologna, I-40126 Bologna, Italy*
 (³) *Boston University, Boston, Massachusetts 02215*
 (⁴) *Brunel University, Uxbridge, Middlesex UB8 3PH, United Kingdom*
 (⁵) *California Institute of Technology, Pasadena, California 91125*
 (⁶) *University of California at Santa Barbara, Santa Barbara, California 93106*
 (⁷) *University of California at Santa Cruz, Santa Cruz, California 95064*
 (⁸) *University of Cincinnati, Cincinnati, Ohio 45221*
 (⁹) *Colorado State University, Fort Collins, Colorado 80523*
 (¹⁰) *University of Colorado, Boulder, Colorado 80309*
 (¹¹) *Columbia University, New York, New York 10027*
 (¹²) *INFN Sezione di Ferrara and Università di Ferrara, I-44100 Ferrara, Italy*
 (¹³) *INFN Lab. Nazionali di Frascati, I-00044 Frascati, Italy*
 (¹⁴) *University of Illinois, Urbana, Illinois 61801*
 (¹⁵) *Lawrence Berkeley Laboratory, University of California, Berkeley, California 94720*
 (¹⁶) *Massachusetts Institute of Technology, Cambridge, Massachusetts 02139*
 (¹⁷) *University of Massachusetts, Amherst, Massachusetts 01003*
 (¹⁸) *University of Mississippi, University, Mississippi 38677*
 (¹⁹) *Moscow State University, Institute of Nuclear Physics, 119899 Moscow, Russia*
 (²⁰) *Nagoya University, Chikusa-ku, Nagoya 464 Japan*
 (²¹) *University of Oregon, Eugene, Oregon 97403*
 (²²) *INFN Sezione di Padova and Università di Padova, I-35100 Padova, Italy*
 (²³) *INFN Sezione di Perugia and Università di Perugia, I-06100 Perugia, Italy*
 (²⁴) *INFN Sezione di Pisa and Università di Pisa, I-56100 Pisa, Italy*
 (²⁵) *Rutgers University, Piscataway, New Jersey 08855*
 (²⁶) *Rutherford Appleton Laboratory, Chilton, Didcot, Oxon OX11 0QX United Kingdom*
 (²⁷) *Sogang University, Seoul, Korea*
 (²⁸) *Stanford Linear Accelerator Center, Stanford University, Stanford, California 94309*
 (²⁹) *University of Tennessee, Knoxville, Tennessee 37996*
 (³⁰) *Tohoku University, Sendai 980 Japan*
 (³¹) *Vanderbilt University, Nashville, Tennessee 37235*
 (³²) *University of Washington, Seattle, Washington 98195*
 (³³) *University of Wisconsin, Madison, Wisconsin 53706*
 (³⁴) *Yale University, New Haven, Connecticut 06511*
 † *Deceased*
 (^a) *Also at the Università di Genova*
 (^b) *Also at the Università di Perugia*

ABSTRACT

We have measured the distributions of the jet energies in $e^+e^- \rightarrow q\bar{q}g$ events, and of the three orientation angles of the event plane, using hadronic Z^0 decays collected in the SLD experiment at SLAC. We find that the data are well described by perturbative QCD incorporating vector gluons. We have also compared our data with models of scalar and tensor gluon production, and discuss limits on the relative contributions of these particles to three-jet production in e^+e^- annihilation.

1. Introduction

The observation of e^+e^- annihilation into final states containing three hadronic jets [1], and their interpretation in terms of the process $e^+e^- \rightarrow q\bar{q}g$, provided the first direct evidence for the existence of the gluon, the gauge boson of the theory of strong interactions, Quantum Chromodynamics (QCD) [2]. Following these initial observations studies of the partition of energy among the three jets were performed at the PETRA and PEP storage rings. Comparison of the data with leading-order QCD predictions, and with a model incorporating the radiation of spin-0 (scalar) gluons, provided qualitative evidence [3] for the spin-1 (vector) nature of the gluon, which is a fundamental element of QCD. Similar studies have since been performed at LEP [4, 5].

An additional interesting observable in three-jet events is the orientation of the event plane w.r.t. the beam direction, which can be described by three Euler angles. These angular distributions were studied first by TASSO [6], and more recently by L3 [4] and DELPHI [7]. Again, the data were compared with the predictions of perturbative QCD and a scalar gluon model, but the Euler angles are less sensitive than the jet energy distributions to the differences between the two cases [4].

Here we present measurements of the jet energy and event plane orientation angle distributions from hadronic decays of Z^0 bosons produced by e^+e^- annihilations at the SLAC Linear Collider (SLC) and recorded in the SLC Large Detector (SLD). We used particle energy deposits measured in the SLD Liquid Argon Calorimeter, which covers 98% of the solid angle, for jet reconstruction. We compare our measured distributions with the predictions of perturbative QCD and a scalar gluon model. In addition, we make the first comparison [8] with a model which comprises spin-2 (tensor) gluons, and discuss limits on the possible relative contributions of scalar and tensor gluons to three-jet production in e^+e^- annihilation.

In Section 2 the observables are defined, and the predictions of perturbative QCD

and of the scalar and tensor gluon models are discussed. We describe the detector, the event trigger, and the selection criteria applied to the data, in Section 3. The three-jet analysis is described in Section 4, and a summary and conclusions are presented in Section 5.

2. Observables and Theoretical Predictions

A. Scaled Jet Energy Distributions

Ordering the three jets in $e^+e^- \rightarrow q\bar{q}g$ according to their energies, $E_1 > E_2 > E_3$, and normalising by the c.m. energy \sqrt{s} , we obtain the scaled jet energies:

$$x_i = \frac{2E_i}{\sqrt{s}} \quad (i = 1, 2, 3), \quad (1)$$

where $x_1 + x_2 + x_3 = 2$. Making a Lorentz boost of the event into the rest frame of jets 2 and 3 the Ellis-Karliner angle θ_{EK} is defined [9] to be the angle between jets 1 and 2 in this frame. For massless partons at tree-level:

$$\cos\theta_{EK} = \frac{x_2 - x_3}{x_1}. \quad (2)$$

The inclusive differential cross section can be calculated to $O(\alpha_s)$ in perturbative QCD incorporating spin-1 (vector) gluons and assuming massless partons [10]:

$$\frac{1}{\sigma} \frac{d^2\sigma^V}{dx_1 dx_2} \propto \frac{x_1^3 + x_2^3 + (2 - x_1 - x_2)^3}{(1 - x_1)(1 - x_2)(x_1 + x_2 - 1)}. \quad (3)$$

One can also consider alternative ‘toy’ models of strong interactions. For a model incorporating spin-0 (scalar) gluons one obtains at leading order at the Z^0 resonance [11]:

$$\frac{1}{\sigma} \frac{d^2\sigma^S}{dx_1 dx_2} \propto \left[\frac{x_1^2(1 - x_1) + x_2^2(1 - x_2) + (2 - x_1 - x_2)^2(x_1 + x_2 - 1)}{(1 - x_1)(1 - x_2)(x_1 + x_2 - 1)} - R \right] \quad (4)$$

where

$$R = \frac{10 \sum_j a_j^2}{\sum_j (v_j^2 + a_j^2)} \quad (5)$$

and a_j and v_j are the axial and vector couplings, respectively, of quark flavor j to the Z^0 . For a model of strong interactions incorporating spin-2 (tensor) gluons (see Appendix) one obtains at leading order:

$$\frac{1}{\sigma} \frac{d^2\sigma^T}{dx_1 dx_2} \propto \frac{(x_1 + x_2 - 1)^3 + (1 - x_1)^3 + (1 - x_2)^3}{(1 - x_1)(1 - x_2)(x_1 + x_2 - 1)}. \quad (6)$$

Singly-differential cross sections for x_1 , x_2 , x_3 or $\cos\theta_{EK}$ were obtained by numerical integrations of Eqs. 3, 4 and 5. These cross sections are shown in Fig. 1; the shapes are different for the vector, scalar and tensor gluon cases.

It is well known that vector particles coupling to quarks in either Abelian or non-Abelian theories allow consistent and renormalizable calculations to all orders in perturbation theory. However, the scalar and tensor gluon models have limited applicability beyond leading order. In the scalar model no symmetry, such as gauge invariance, exists to prevent the gluons from acquiring mass. In the tensor case the model is non-renormalizable (see Appendix), so that higher order predictions are not physically meaningful. Given these difficulties we limit ourselves to the leading-order expressions for 3-jet event production in these two cases. In the vector case we do consider the influence of higher-order corrections to the leading-order predictions. We also assume that the transformation of the partons in 3-jet events into the observed hadrons is independent of the gluon spin.

B. Event Plane Orientation

The orientation of the three-jet event plane can be described by the angles θ , θ_N and χ illustrated in Fig. 2. When no explicit quark, antiquark or gluon jet identification is made, θ is the polar angle of the most energetic jet w.r.t. the electron beam direction, θ_N is the polar angle of the normal to the event plane w.r.t. the electron beam direction, and χ is the angle between the event plane and the plane containing the electron beam and the most energetic jet. The distributions of these angles may be written [11]:

$$\frac{d\sigma}{d\cos\theta} \propto 1 + \alpha(T)\cos^2\theta \quad (7)$$

$$\frac{d\sigma}{d\cos\theta_N} \propto 1 + \alpha_N(T)\cos^2\theta_N \quad (8)$$

$$\frac{d\sigma}{d\chi} \propto 1 + \beta(T)\cos 2\chi \quad (9)$$

where T is the thrust value [12] of the event. The coefficients $\alpha(T)$, $\alpha_N(T)$ and $\beta(T)$ depend on the gluon spin; they are shown in Fig. 16 for leading-order calculations incorporating vector, scalar and tensor gluons. In perturbative QCD $\mathcal{O}(\alpha_s^2)$ corrections to the leading-order result have been calculated and are small [13].

In Z^0 decay events produced with longitudinally-polarized electrons an additional term $\beta_N S_Z \cos\theta_N$, representing a correlation between the event-plane orientation and the Z^0 spin direction, should be added to eq. (8). For Standard Model processes the

correlation parameter β_N is expected [14] to be of order 10^{-5} , which is well below our current experimental sensitivity [15]. In this analysis we have ignored information on the helicity of the electron beam and are hence insensitive to a term in eq. (8) linear in $\cos\theta_N$.

3. Apparatus and Hadronic Event Selection

The e^+e^- annihilation events produced at the Z^0 resonance by the SLC in the 1993 run were recorded using the SLD. A general description of the SLD can be found elsewhere [16]. The analysis presented here used particle energy deposits measured in the Liquid Argon Calorimeter (LAC) [17], which contains both electromagnetic and hadronic sections, and in the Warm Iron Calorimeter [18]. The trigger for hadronic events required a total LAC electromagnetic energy greater than 12 GeV.

Clusters were formed from the localized energy depositions in the LAC; energy depositions consistent with background muons produced upstream in the accelerator were identified and removed [19]. The measured cluster energies were then corrected [8] for the response of the LAC, which varies with polar angle θ due to the material of the inner detector components as well as the thinner calorimeter coverage at the endcap-barrel interface, using a detailed Monte Carlo simulation of the detector. We first verified that the measured energy of clusters in each polar-angle bin, integrated over all selected clusters in all selected hadronic events, was well described by the simulation. Next, the ratio of simulated cluster energy to generated particle energy was calculated for each cluster. This ratio was averaged over all clusters in each polar-angle bin to yield the response function $r(\theta)$. Finally, the measured energy of each cluster in the data was weighted by $1/r(\theta)$. The normalised r.m.s. deviation of the distribution of the total cluster energy in hadronic events was 21% before, and 16.5% after, application of this procedure [8].

Corrected clusters were then required to have a non-zero electromagnetic energy component and a total energy E_{cl} of at least 100 MeV. For each event the total cluster energy E_{tot} , energy imbalance $\Sigma|\vec{E}_{cl}|/E_{tot}$, and thrust axis polar angle θ_T [12] were calculated from the selected corrected clusters. Events with $|\cos\theta_T| \leq 0.8$ ($|\cos\theta_T| \geq 0.8$) were then required to contain at least 8 (11) such clusters, to have $E_{tot} > 15$ GeV, and to have $\Sigma|\vec{E}_{cl}|/E_{tot} < 0.6$. From our 1993 data sample approximately 51,000 events passed these cuts. The efficiency for selecting hadronic events was estimated to be $92 \pm 2\%$, with an estimated background in the selected sample of $0.4 \pm 0.2\%$ [20], dominated by $Z^0 \rightarrow \tau^+\tau^-$ and $Z^0 \rightarrow e^+e^-$ events.

4. Data Analysis

Jets were reconstructed from selected LAC clusters in selected hadronic events. The JADE jet-finding algorithm [21] was used, with a scaled invariant mass cutoff value $y_c = 0.02$, to identify a sample of 22,114 3-jet events. This y_c value maximises the rate of events classified as 3-jet final states; other values of y_c were also considered and found not to affect the conclusions of this study. A non-zero sum of the three jet momenta can be induced in the selected events by particle losses due to the acceptance and inefficiency of the detector, and by jet energy resolution effects. This was corrected by rescaling the measured jet momenta \vec{P}_i ($i = 1, 2, 3$) according to:

$$P_i^{j'} = P_i^j - R^j |P_i^j| \quad (10)$$

where P_i^j is the j -th momentum component of jet i , $j = x, y, z$, and

$$R^j = \frac{\sum_{i=1}^3 P_i^j}{\sum_{i=1}^3 |P_i^j|}. \quad (11)$$

The jet energy components were then rescaled according to:

$$E_i' = \frac{|\vec{P}_i'|}{|\vec{P}_i|} E_i \quad (12)$$

This procedure resulted in a slight improvement in the experimental resolution of the scaled jet energies x_i [8].

A. Scaled Jet Energy Distributions

The measured distributions of the three scaled jet energies x_1 , x_2 , x_3 , and the Ellis-Karliner angle θ_{EK} , are shown in Fig. 3. Also shown in Fig. 3 are the predictions of the HERWIG 5.7 [22] Monte Carlo program for the simulation of hadronic decays of Z^0 bosons, combined with a simulation of the SLD and the same selection and analysis cuts as applied to the real data. The simulation describes the data well.

For each observable X , the experimental distribution $D_{SLD}^{data}(X)$ was then corrected for the effects of selection cuts, detector acceptance, efficiency, resolution, particle decays and interactions within the detector, and for initial state photon radiation, using bin-by-bin correction factors $C_D(X)$:

$$C_D(X)_m = \frac{D_{hadron}^{MC}(X)_m}{D_{SLD}^{MC}(X)_m}, \quad (13)$$

where: m is the bin index; $D_{SLD}^{MC}(X)_m$ is the content of bin m of the distribution obtained from reconstructed clusters in Monte Carlo events after simulation of the

detector; and $D_{hadron}^{MC}(X)_i$ is that from all generated particles with lifetimes greater than 3×10^{-10} s in Monte Carlo events with no SLD simulation and no initial state radiation. The bin widths were chosen from the estimated experimental resolution so as to minimize bin-to-bin migration effects. The $C_D(X)$ were calculated from events generated with HERWIG 5.7 using default parameter values [22]. The *hadron level* distributions are then given by

$$D_{hadron}^{data}(X)_m = C_D(X)_m \cdot D_{SLD}^{data}(X)_m. \quad (14)$$

Experimental systematic errors arising from uncertainties in modelling the detector were estimated by varying the event selection criteria over wide ranges, and by varying the cluster energy response corrections in the detector simulation [8]. In each case the correction factors $C_D(X)$, and hence the corrected data distributions $D_{hadron}^{data}(X)$, were rederived. The correction factors $C_D(X)$ are shown in Figs. 4(b)–7(b); the errors comprise the sum in quadrature of the statistical component from the finite size of the Monte Carlo event sample, and the systematic uncertainty. It can be seen that the $C_D(X)$ are close to unity and slowly-varying, except near the boundaries of phase-space. The hadron level data are listed in Tables I–IV, together with statistical and systematic errors; the central values represent the data corrected by the central values of the correction factors.

Before they can be compared with parton-level predictions the data must be corrected for the effects of hadronization. In the absence of a complete theoretical calculation, the phenomenological models implemented in JETSET 7.4 [23] and HERWIG 5.7 represent our best description of the hadronization process, and are not based upon a particular choice of the gluon spin. These models have been compared extensively with, and tuned to, $e^+e^- \rightarrow$ hadrons data at the Z^0 resonance [24], as well as data at $W \sim 35$ GeV from the PETRA and PEP storage rings [25]. We find that they provide a good description of our data in terms of the observables presented here (Fig. 3) and other hadronic event shape observables [26], and hence employ them to calculate hadronization correction factors. The HERWIG parameters were left at their default values. Several of the JETSET parameters were set to values determined from our own optimisation to hadronic Z^0 data; these are given in Table V.

The hadronization correction procedure is similar to that described above for the detector effects. Bin-by-bin correction factors

$$C_H(X)_m = \frac{D_{parton}^{MC}(X)_m}{D_{hadron}^{MC}(X)_m}, \quad (15)$$

where $D_{parton}^{MC}(X)_m$ is the content of bin m of the distribution obtained from Monte Carlo events generated at the parton level, were calculated and applied to the hadron

level data distributions $D_{hadron}^{data}(X)_m$ to obtain the *parton level* corrected data:

$$D_{parton}^{data}(X)_m = C_H(X)_m \cdot D_{hadron}^{data}(X)_m. \quad (16)$$

For each bin the average of the JETSET– and HERWIG–derived values was used as the central value of the correction factor, and the difference between this value and the extrema was assigned as a symmetric hadronization uncertainty. The correction factors $C_H(X)$ are shown in Figs. 4(c)–7(c); the errors comprise the sum in quadrature of the statistical component from the finite size of the Monte Carlo event sample, and the systematic uncertainty. It can be seen that the $C_H(X)$ are within 10% of unity and are slowly-varying, except near the boundaries of phase space. The fully-corrected data are shown in Figs. 4(a)–7(a); the data points correspond to the central values of the correction factors, and the errors shown comprise the statistical and total systematic components added in quadrature. These results are in agreement with an analysis of our 1992 data sample using charged tracks for jet reconstruction [27].

We first compare the data with QCD predictions from $O(\alpha_s)$ and $O(\alpha_s^2)$ perturbation theory, and from parton shower (PS) models. For this purpose we used the JETSET 7.4 $O(\alpha_s)$ matrix element, $O(\alpha_s^2)$ matrix element, and PS options, and the HERWIG 5.7 PS, and generated events at the parton level. In each case all parameters were left at their default values [22, 23], with the exception of the JETSET parton shower parameters listed in Table V. The QCD scale parameter values used were $\Lambda = 1.0$ GeV ($O(\alpha_s)$), 0.25 GeV ($O(\alpha_s^2)$), 0.26 GeV (JETSET PS) and 0.18 GeV (HERWIG PS). The shapes of the x_1 , x_2 , x_3 and $\cos\theta_{EK}$ distributions do not depend on Λ at $O(\alpha_s)$, and only weakly so at higher order. The resulting predictions for x_1 , x_2 , x_3 and $\cos\theta_{EK}$ are shown in Figs. 4(a) – 7(a). These results represent Monte Carlo integrations of the respective QCD formulae and are hence equivalent to analytic or numerical QCD results based on the same formulae; in the $O(\alpha_s)$ case we have checked explicitly that JETSET reproduces the numerical results of the analytic calculation described in Section 2.

The $O(\alpha_s)$ calculation describes the data reasonably well, although small discrepancies in the details of the shapes of the distributions are apparent and the χ^2 for the comparison between data and MC is poor (Table VI). The $O(\alpha_s^2)$ calculation describes the x_1 , x_2 and x_3 data distributions better, but the description of the $\cos\theta_{EK}$ distribution is slightly worse; this is difficult to see directly in Figs. 4(a)–7(a), but is evident from the χ^2 values for the data–MC comparisons (Table VI). Both parton shower calculations describe the data better than either the $O(\alpha_s)$ or $O(\alpha_s^2)$ calculations and yield relatively good χ^2 values (Table VI). This improvement in the quality of description of the data between the $O(\alpha_s)$ and parton shower calculations can be interpreted as an indication of the contribution of multiple soft gluon emission to the fine details of

the shapes of the distributions. In fact for all calculations the largest discrepancies, at the level of at most 10%, arise in the regions $x_1 > 0.98$, $x_2 > 0.93$, $x_3 < 0.09$ and $\cos\theta_{EK} > 0.9$, near the boundaries of phase space where soft and collinear divergences are expected to be large and to require resummation in QCD perturbation theory [28]; such resummation has not been performed for the observables considered here.

For each observable we chose a range such that the detector and hadronization correction factors are close to unity, $0.8 < C_D(X), C_H(X) < 1.2$, have small uncertainty, $\Delta C_D(X), \Delta C_H(X) < 0.2$, and are slowly-varying (see Figs. 4–7). The ranges are: $0.688 < x_1 < 0.976$, $x_2 < 0.93$, $x_3 > 0.09$ and $\cos\theta_{EK} < 0.9$; they exclude the phase-space boundary regions. Within these ranges the comparison between data and calculations yields significantly improved χ^2 values (values in parentheses in Table VI); the $O(\alpha_s^2)$ calculation has acceptable χ^2 values and those for both parton shower models are typically slightly better. These results support the notion that QCD, incorporating vector gluons, is the correct theory of strong interactions.

We now consider alternative models of strong interactions, incorporating scalar and tensor gluons, discussed in Section 2. Since these model calculations are at leading order in perturbation theory we also consider first the vector gluon (QCD) case at the same order. The data within the selected ranges are shown in Fig. 8; from comparison with the raw data (Fig. 3) it is apparent that the shapes of the distributions are barely affected by the detector and hadronization corrections. The leading-order scalar, vector and tensor gluon predictions, normalised to the data within the same ranges, are also shown in Fig. 8. The vector calculation clearly provides the best description of the data; neither the scalar nor tensor cases predicts the correct shape for any of the observables. The χ^2 values for the comparisons are given in Table VII. This represents the first comparison of a tensor gluon calculation with experimental data.

It is interesting to consider whether the data allow an admixture of contributions from the different gluon spin hypotheses. For this purpose we performed simultaneous fits to a linear combination of the vector (V) + scalar (S) + tensor (T) predictions, allowing the relative normalisations to vary according to:

$$(1 - a - b)V \quad + \quad aS \quad + \quad bT \tag{17}$$

where a and b are free parameters determined from the fit. For the vector contribution we used in turn the $O(\alpha_s)$, $O(\alpha_s^2)$, JETSET PS and HERWIG PS calculations. In all cases the fit to the distribution of each observable yielded a slightly lower χ^2 value than the vector-only fit. We found that the allowed contributions of scalar and tensor gluons depend upon the order of the vector calculation used, as well as on the observable. The largest allowed scalar contribution was $a = 0.11$ from the fit to $\cos\theta_{EK}$ using the $O(\alpha_s^2)$ calculation. The largest allowed tensor contribution was $b = 0.31$ from the fit

to x_1 using the $O(\alpha_s)$ calculation. The smallest allowed contributions were a and $b < 0.001$ from the fit to x_1 using the HERWIG PS.

Any pair of the observables x_1, x_2, x_3 and $\cos\theta_{EK}$ may be taken to be independent variables, subject to the overall constraint $x_1 + x_2 + x_3 = 2$. Therefore, in order to utilise more information, we also performed fits of Eq. 17 simultaneously to the x_2 and x_3 distributions. We found the relative S, V and T contributions and the $\chi^2/d.o.f.$ values to be comparable with those from the fits to x_2 alone.

B. Event Plane Orientation

We now consider the three Euler angles that describe the orientation of the event plane: θ , θ_N , and χ (Fig. 2). The analysis procedure is similar to that described in the previous section. The measured distributions of these angles are shown in Fig. 9, together with the predictions of HERWIG 5.7, combined with a simulation of the SLD and the same selection and analysis cuts as applied to the data. The simulations describe the data reasonably well. The data distributions were then corrected for the effects of selection cuts, detector acceptance, efficiency, and resolution, particle decays and interactions within the detector, and for initial state photon radiation using bin-by-bin correction factors determined from the Monte Carlo simulation. The correction factors C_D are shown in Figs. 10(b)–12(b); the errors comprise the sum in quadrature of the statistical component from the finite size of the Monte Carlo event sample, and the systematic uncertainty derived as described in the previous section. The hadron level data are listed in Tables VIII–X, together with statistical and systematic errors; the central values represent the data corrected by the central values of the correction factors.

The data were further corrected bin-by-bin for the effects of hadronisation. The hadronisation correction factors are shown in Figs. 10(c)–12(c); the errors comprise the sum in quadrature of the statistical component from the finite size of the Monte Carlo event sample, and the systematic uncertainty. The fully-corrected data are shown in Figs. 10(a)–12(a); the data points correspond to the central values of the correction factors, and the errors shown comprise the statistical and total systematic components added in quadrature. Also shown in Figs. 10(a)–12(a) are the parton-level predictions of the JETSET 7.4 $O(\alpha_s)$ matrix element, $O(\alpha_s^2)$ matrix element, and parton shower options, and the HERWIG 5.7 parton shower. All calculations describe the data well, and higher-order corrections to the $O(\alpha_s)$ predictions are seen to be small.

The data were divided into four samples according to the thrust values of the events: (i) $0.70 < T < 0.80$, (ii) $0.80 < T < 0.85$, (iii) $0.85 < T < 0.90$ and (iv) $0.90 < T < 0.95$. The distributions of $\cos\theta$, $\cos\theta_N$ and χ are shown for these four ranges in Figs. 13, 14 and 15 respectively. Also shown in these figures are fits of

Eqs. (7), (8) and (9) (Section 2), where the parameters $\alpha(T)$, $\alpha_N(T)$ and $\beta(T)$ were determined, respectively, from the fits. The fitted values of these parameters are listed in Table XI, and are shown in Fig. 16, where they are compared with the leading-order QCD predictions and with the predictions of the scalar and tensor gluon models. Values of χ^2 for these comparisons are given in Table XII. The data are in agreement with the QCD predictions, and the scalar and tensor gluon predictions are disfavoured. It should be noted, however, that the event plane orientation angle distributions are less sensitive to the different gluon spin cases than are the jet energy distributions discussed in the previous section.

5. Conclusions

We have measured distributions of the jet energies, and of the orientation angles of the event plane, in $e^+e^- \rightarrow Z^0 \rightarrow$ three-jet events recorded in the SLD experiment at SLAC. Our measurements of these quantities are consistent with those from other experiments [4, 5, 7] at the Z^0 resonance. We have compared our measurements with QCD predictions and with models of strong interactions incorporating scalar or tensor gluons; this represents the first comparison with a tensor gluon calculation.

The leading-order vector gluon (QCD) calculation describes the basic shape of the scaled jet energy distributions, and addition of higher-order perturbative contributions leads to a reasonable description of the finer details of these distributions, provided the regions of phase space are avoided where soft and collinear singularities need to be resummed. One may speculate that the addition of as yet uncalculated higher-order QCD contributions may yield further improvement. The shapes of the jet energy distributions cannot be described by leading-order models incorporating either scalar or tensor gluons alone. However, the *ad hoc* addition of leading-order contributions from scalar and tensor gluons, each with arbitrary relative weight, to the QCD predictions can also improve the description of the data; even for the QCD parton shower calculations slightly better fit qualities are obtained with such contributions included. The allowed relative contributions of scalar and tensor gluons depend upon the order of the vector calculation, as well as the observable; the smallest allowed contribution of 0.1% for both scalar and tensor gluons is obtained with the HERWIG parton shower fit to the scaled energy of the most energetic jet.

The event plane orientation angles are well described by $O(\alpha_s)$ QCD and higher-order corrections are small. These quantities are less sensitive to the gluon spin than the jet energies, but the data disfavor the scalar and tensor hypotheses.

6. Acknowledgements

We thank Lance Dixon for contributions to the tensor gluon model. We thank the personnel of the SLAC accelerator department and the technical staffs of our collaborating institutions for their efforts which resulted in the successful operation of the SLC and the SLD.

Appendix: Tensor Gluon Model

Since the tensor gluon toy model is new, whereas the vector and scalar cases have been studied in detail in the literature, we discuss briefly how Eq. 6 was obtained.

The only well-known theory involving the exchange of massless, spin-2 gauge fields is the quantized version of General Relativity, which is both highly non-linear and non-renormalizable. To obtain a simple parallel model for tensor gluons, which couple only to color non-singlet sources, we begin by linearizing the theory of quantum gravity based on General Relativity by keeping only the lowest order terms in the coupling and by ignoring the tensor field self-interactions [29]. Although now linear, the theory remains non-renormalizable, as will be the tensor gluon model, which should be viewed only as a toy model against which to test the predictions of QCD.

If tensor gluons behaved in the same way as gravitons one could write down the complete gauge-invariant amplitude for the tree-level process $Z^0 \rightarrow q\bar{q}g$. The various contributions arise from a set of four Feynman diagrams: the usual two which involve gluon bremsstrahlung from the q or \bar{q} in the final state, the bremsstrahlung of a tensor gluon from the Z^0 in the initial state, producing an off-shell Z^0 which ‘decays’ to $q\bar{q}$, and finally a new $Z^0 q\bar{q}g$ contact interaction. We need to remove or modify the $Z^0 Z^0 g$ piece of the amplitude as the Z^0 is known phenomenologically not to carry a color charge.

We consider two possible approaches to this problem. In the first instance we surrender the possibility of a gauge symmetry for the tensor gluon theory and omit the diagram involving the $Z^0 Z^0 g$ vertex. (We note that the scalar gluon model is also not a gauge theory.) In this case, using the Feynman gauge for the tensor gluon, we arrive at the distribution given in Eq. 6. A second possibility is to mimic the quantum gravity theory as far as possible and include the $Z^0 Z^0 g$ diagram in a modified form. To do this we extend the particle spectrum of the Standard Model by introducing a color-octet partner to the Z^0 , Z_8^0 , which is degenerate with the Z^0 and couples to quarks in exactly the same way as does the Z^0 , except for the presence of color generators. The problematic $Z^0 Z^0 g$ vertex is now replaced by the $Z^0 Z_8^0 g$ coupling. In this case we

arrive at a form for the tensor distribution given by [30]:

$$\frac{1}{\sigma} \frac{d^2\sigma^T}{dx_1 dx_2} \propto \frac{(x_1 + x_2 - 1)(x_1^2 + x_2^2)}{(2 - x_1 - x_2)^2} + \frac{(1 - x_2)(x_1^2 + (2 - x_1 - x_2)^2)}{x_2^2} + \frac{(1 - x_1)(x_2^2 + (2 - x_1 - x_2)^2)}{x_1^2}, \quad (18)$$

which, apart from the overall normalisation, is the same as that for graviton radiation in Z^0 decays. Although algebraically different, this form yields numerically similar results to Eq. 6 (Fig. 17).

In the analysis presented in the text the comparison of the tensor model with the data is based on Eq. 6. It is clear from Fig. 17, however, that our conclusions would not differ if Eq. 18 had been chosen instead.

References

- [1] TASSO Collab., R. Brandelik *et al.*, Phys. Lett. **86B** (1979) 243.
Mark J Collab., D.P. Barber *et al.*, Phys. Rev. Lett. **43** (1979) 830.
PLUTO Collab., Ch. Berger *et al.*, Phys. Lett. **86B** (1979) 418.
JADE Collab., W. Bartel *et al.*, Phys. Lett. **91B** (1980) 142.
- [2] H. Fritzsche, M. Gell-Mann, and H. Leutwyler, Phys. Lett. **B47** (1973) 365.
D. J. Gross and F. Wilczek, Phys. Rev. Lett. **30** (1973) 1343.
H. D. Politzer, Phys. Rev. Lett. **30** (1973) 1346.
- [3] TASSO Collab., R. Brandelik *et al.*, Phys. Lett. **B97** (1980) 453.
PLUTO Collab., C. Berger *et al.*, Phys. Lett. **B97** (1980) 459.
CELLO Collab., H.-J. Behrend *et al.*, Phys. Lett. **B110** (1982) 329.
- [4] L3 Collab., B. Adeva *et al.*, Phys. Lett. **B263** (1991) 551.
- [5] OPAL Collab., G. Alexander *et al.*, Z. Phys. **C52** (1991) 543.
- [6] TASSO Collab., W. Braunschweig *et al.*, Z. Phys. **C47** (1990) 181.
- [7] DELPHI Collab., P. Abreu *et al.*, Phys. Lett. **B274** (1992) 498.
- [8] H. Hwang, Univ. of Oregon Ph.D. thesis; SLAC Report 453 (1994).
- [9] J. Ellis, I. Karliner, Nucl. Phys. **B148** (1979) 141.
- [10] See *eg.* G. Kramer, Springer Tracts in Modern Physics, Vol. 102 (1984) p.39.
- [11] P. Hoyer, P. Osland, H.G. Sander, T.F. Walsh and P.M. Zerwas, Nucl. Phys. **B161** (1979) 349;
E. Laermann, K.H. Streng and P.M. Zerwas, Z. Phys. **C3** (1980) 289; *erratum ibid* **C52** (1991) 352.
- [12] S. Brandt *et al.*, Phys. Lett. **12** (1964) 57.
E. Farhi, Phys. Rev. Lett. **39** (1977) 1587.
- [13] J. Körner, G.A. Schuler, F. Barreiro, Phys. Lett. **B188** (1987) 272.
- [14] A. Brandenburg, L. Dixon, Y. Shadmi, Phys. Rev. **D53** (1996) 1264.
- [15] SLD Collab., K. Abe *et al.*, Phys. Rev. Lett. **75** (1995) 4173.
- [16] SLD Design Report, SLAC Report 273 (1984).

- [17] D. Axen *et al.*, Nucl. Inst. Meth. **A328** (1993) 472.
- [18] A. C. Benvenuti *et al.*, Nucl. Inst. Meth. **A290** (1990) 353.
- [19] J.M. Yamartino, M.I.T. Ph.D. Thesis, SLAC Report 426 (1994).
- [20] SLD Collab., K. Abe *et al.*, Phys. Rev. Lett. **73** (1994) 25.
- [21] JADE Collab., W. Bartel *et al.*, Z. Phys. **C33** (1986) 23.
- [22] G. Marchesini *et al.*, Comp. Phys. Comm. **67** (1992) 465.
- [23] T. Sjöstrand, CERN-TH-7112/93 (1993).
- [24] OPAL Collab., M. Z. Akrawy *et al.*, Z. Phys. **C47** (1990) 505,
L3 Collab., B. Adeva *et al.*, Z. Phys. **C55** (1992) 39,
ALEPH Collab., D. Buskulic *et al.*, Z. Phys. **C55** (1992) 209.
- [25] Mark II Collab., A. Petersen *et al.*, Phys. Rev. **D37** (1988) 1,
TASSO Collab., W. Braunschweig *et al.*, Z. Phys. **C41** (1988) 359,
P. N. Burrows, Z. Phys. **C41** (1988) 375.
- [26] SLD Collab., K. Abe *et al.*, Phys. Rev. **D51** (1995) 962.
- [27] C.-G. Fan, Univ. of Colorado Ph.D. Thesis, SLAC Report 424 (1994).
- [28] S. Catani, L. Trentadue, G. Turnock, B.R. Webber, Nucl. Phys. **B407** (1993) 3.
- [29] For the details of this approach, see S.Y. Choi, J. Lee, J.S. Shim and H.S. Song,
Phys. Rev. **D48** (1993) 769, and references therein.
- [30] L. Dixon, private communications.

x_1	$\frac{1}{\sigma_{3-jet}} \frac{d\sigma}{dx_1}$	stat.	exp. syst.
0.676	0.025	0.007	0.008
0.700	0.072	0.016	0.018
0.724	0.133	0.018	0.022
0.748	0.260	0.025	0.033
0.772	0.423	0.028	0.044
0.796	0.530	0.032	0.044
0.820	0.749	0.039	0.048
0.844	1.065	0.048	0.061
0.868	1.603	0.056	0.071
0.892	2.351	0.069	0.088
0.916	3.83	0.09	0.11
0.940	6.74	0.11	0.14
0.964	13.80	0.17	0.27
0.988	9.08	0.13	0.17

Table I. The measured scaled jet energy of the highest-energy jet in 3-jet events. The data were corrected for detector effects and for initial state photon radiation. The first error is statistical, and the second represents the experimental systematic uncertainty.

x_2	$\frac{1}{\sigma_{3-jet}} \frac{d\sigma}{dx_2}$	stat.	exp. syst.
0.5275	0.490	0.024	0.031
0.5625	1.031	0.039	0.050
0.5975	1.267	0.043	0.050
0.6325	1.356	0.044	0.051
0.6675	1.546	0.048	0.058
0.7025	1.689	0.048	0.057
0.7375	1.815	0.051	0.068
0.7725	1.938	0.053	0.061
0.8075	2.089	0.055	0.063
0.8425	2.619	0.060	0.071
0.8775	2.966	0.063	0.074
0.9125	3.391	0.064	0.082
0.9475	3.813	0.062	0.079
0.9825	2.205	0.056	0.075

Table II. The measured scaled jet energy of the second highest-energy jet in 3-jet events. The data were corrected for detector effects and for initial state photon radiation. The first error is statistical, and the second represents the experimental systematic uncertainty.

x_3	$\frac{1}{\sigma_{3-jet}} \frac{d\sigma}{dx_3}$	stat.	exp. syst.
0.0225	1.095	0.037	0.050
0.0675	2.622	0.044	0.059
0.1125	2.632	0.048	0.069
0.1575	2.340	0.049	0.060
0.2025	2.228	0.049	0.060
0.2475	1.878	0.046	0.054
0.2925	1.645	0.043	0.052
0.3375	1.502	0.040	0.051
0.3825	1.386	0.040	0.049
0.4275	1.400	0.039	0.048
0.4725	1.356	0.038	0.045
0.5175	1.090	0.035	0.043
0.5625	0.378	0.022	0.028
0.6075	0.188	0.016	0.022
0.6525	0.037	0.008	0.009

Table III. The measured scaled jet energy of the lowest-energy jet in 3-jet events. The data were corrected for detector effects and for initial state photon radiation. The first error is statistical, and the second represents the experimental systematic uncertainty.

$\cos\theta_{EK}$	$\frac{1}{\sigma_{3-jet}} \frac{d\sigma}{d\cos\theta_{EK}}$	stat.	exp. syst.
0.025	0.689	0.028	0.032
0.075	0.692	0.028	0.032
0.125	0.678	0.027	0.035
0.175	0.669	0.027	0.032
0.225	0.671	0.026	0.030
0.275	0.716	0.027	0.031
0.325	0.718	0.026	0.034
0.375	0.733	0.028	0.043
0.425	0.819	0.028	0.034
0.475	0.803	0.029	0.037
0.525	0.835	0.029	0.035
0.575	0.906	0.030	0.036
0.625	1.055	0.032	0.038
0.675	1.207	0.034	0.047
0.725	1.290	0.034	0.041
0.775	1.420	0.035	0.047
0.825	1.507	0.035	0.056
0.875	1.700	0.035	0.043
0.925	1.696	0.032	0.043
0.975	0.776	0.029	0.039

Table IV. The measured Ellis-Karliner angle distribution in 3-jet events. The data were corrected for detector effects and for initial state photon radiation. The first error is statistical, and the second represents the experimental systematic uncertainty.

Parameter	Variable Name	Default	Optimised
Λ_{QCD}	PARJ(81)	0.29 GeV	0.26 GeV
σ_q	PARJ(21)	0.36 GeV/ c	0.39 GeV/ c
a	PARJ(41)	0.3	0.18
b	PARJ(42)	0.58 GeV $^{-2}$	0.34 GeV $^{-2}$
ϵ_c	PARJ(54)	-0.05	-0.06
ϵ_b	PARJ(55)	-0.005	-0.006
diquark prob.	PARJ(1)	0.10	0.08
s quark prob.	PARJ(2)	0.30	0.28
s diquark prob.	PARJ(3)	0.40	0.60
V meson prob. (u,d)	PARJ(11)	0.50	0.50
V meson prob. (s)	PARJ(12)	0.60	0.45
V meson prob. (c,b)	PARJ(13)	0.75	0.53
η' prob.	PARJ(26)	0.40	0.20

Table V. Parameters in JETSET 7.4 that were changed from default values (see text).

Distribution	# bins	JETSET $O(\alpha_s)$	JETSET $O(\alpha_s^2)$	JETSET PS	HERWIG PS
x_1	14 (12)	88.2 (72.6)	38.5 (26.3)	13.5 (6.3)	11.2 (10.6)
x_2	14 (12)	37.8 (20.0)	36.8 (12.2)	34.9 (21.0)	15.2 (6.5)
x_3	15 (13)	92.9 (49.8)	86.5 (29.6)	22.3 (17.5)	25.7 (11.8)
$\cos\theta_{EK}$	20 (18)	60.6 (26.3)	86.2 (44.6)	15.8 (9.0)	48.2 (30.2)

Table VI. Numbers of bins and χ^2 values for comparison between fully corrected data and parton-level QCD Monte Carlo calculations. Values in parentheses are for the restricted ranges which exclude the regions where soft and collinear contributions are expected to be large.

Distribution	# bins	Vector	Scalar	Tensor
x_1	12	45.2	1116.4	141.9
x_2	12	33.5	1321.7	490.6
x_3	13	39.9	2011.4	546.9
$\cos\theta_{EK}$	18	19.5	1684.0	772.1

Table VII. Numbers of bins and χ^2 values for comparison between fully corrected data and leading-order vector (QCD), scalar, and tensor gluon calculations.

$\cos\theta$	$\frac{1}{\sigma_{3-jet}} \frac{d\sigma}{d\cos\theta}$	stat.	exp. syst.
0.071	0.792	0.021	0.031
0.214	0.822	0.023	0.031
0.357	0.853	0.023	0.030
0.500	0.982	0.024	0.033
0.643	1.088	0.026	0.031
0.786	1.135	0.028	0.035
0.929	1.306	0.035	0.090

Table VIII. The measured polar angle w.r.t. the electron beam of the highest-energy jet in 3-jet events. The data were corrected for detector effects and for initial state photon radiation. The first error is statistical, and the second represents the experimental systematic uncertainty.

$\cos\theta_N$	$\frac{1}{\sigma_{3-jet}} \frac{d\sigma}{d\cos\theta_N}$	stat.	exp. syst.
0.071	1.159	0.034	0.076
0.214	1.079	0.029	0.046
0.357	1.110	0.026	0.029
0.500	0.969	0.025	0.028
0.643	0.967	0.025	0.035
0.786	0.917	0.023	0.036
0.929	0.804	0.020	0.030

Table IX. The measured polar angle w.r.t. the electron beam of the normal to the three-jet plane. The data were corrected for detector effects and for initial state photon radiation. The first error is statistical, and the second represents the experimental systematic uncertainty.

χ (rad.)	$\frac{1}{\sigma_{3-jet}} \frac{d\sigma}{d\chi}$	stat.	exp. syst.
0.112	0.671	0.025	0.034
0.336	0.644	0.025	0.027
0.561	0.633	0.025	0.026
0.785	0.642	0.024	0.025
1.009	0.635	0.023	0.025
1.234	0.592	0.021	0.023
1.458	0.645	0.021	0.023

Table X. The measured angle between the event plane and the plane containing the highest-energy jet and the electron beam. The data were corrected for detector effects and for initial state photon radiation. The first error is statistical, and the second represents the experimental systematic uncertainty.

Thrust range	$\alpha(T)$	χ^2	$\alpha_N(T)$	χ^2	$\beta(T)$	χ^2
$0.7 < T < 0.8$	0.61 ± 0.18	6.1	-0.42 ± 0.10	1.9	0.090 ± 0.069	5.4
$0.8 < T < 0.85$	0.83 ± 0.19	3.6	-0.31 ± 0.11	0.6	0.034 ± 0.071	3.3
$0.85 < T < 0.9$	0.82 ± 0.12	8.3	-0.33 ± 0.07	7.8	0.004 ± 0.041	4.4
$0.9 < T < 0.95$	0.81 ± 0.09	2.6	-0.26 ± 0.06	6.8	-0.033 ± 0.030	0.5

Table XI. Thrust ranges, values and errors of the fit parameters α , α_N and β , and χ^2 values for the fits. For each fitted observable there are 7 bins.

Gluon spin	$\alpha(T)$	$\alpha_N(T)$	$\beta(T)$
Vector	3.0	2.8	2.4
Scalar	17.4	38.0	8.8
Tensor	7.3	5.7	4.4

Table XII. Values of χ^2 for comparisons between the predictions including vector, scalar or tensor gluons for the coefficients $\alpha(T)$, $\alpha_N(T)$ and $\beta(T)$ and the measured values (Fig. 16).

Figure captions

Figure 1. Leading-order calculations, incorporating vector (solid), scalar (long dashed), and tensor (short dashed) gluons, of distributions of: (a) scaled energy of the highest-energy jet; (b) scaled energy of the second highest-energy jet; (c) scaled energy of the lowest-energy jet; (d) the Ellis-Karliner angle.

Figure 2. Definition of the Euler angles θ , θ_N and χ that describe the orientation of the event plane.

Figure 3. Measured distributions (dots) of: (a) scaled energy of the highest-energy jet; (b) scaled energy of the second highest-energy jet; (c) scaled energy of the lowest-energy jet; (d) the Ellis-Karliner angle. The errors are statistical only. The predictions of a Monte Carlo simulation are shown as solid histograms.

Figure 4. (a) The measured distribution (dots) of the scaled energy of the highest-energy jet, fully-corrected to the parton level, compared with QCD Monte Carlo calculations. The errors comprise the total statistical and systematic components added in quadrature. The correction factors for detector effects and initial-state radiation (b) and for hadronisation effects (c); the inner error bars show the statistical component and the outer error bars the total uncertainty.

Figure 5. (a) The measured distribution (dots) of the scaled energy of the second highest-energy jet, fully-corrected to the parton level, compared with QCD Monte Carlo calculations. The errors comprise the total statistical and systematic components added in quadrature. The correction factors for detector effects and initial-state radiation (b) and for hadronisation effects (c); the inner error bars show the statistical component and the outer error bars the total uncertainty.

Figure 6. (a) The measured distribution (dots) of the scaled energy of the lowest-energy jet, fully-corrected to the parton level, compared with QCD Monte Carlo calculations. The errors comprise the total statistical and systematic components added in quadrature. The correction factors for detector effects and initial-state radiation (b) and for hadronisation effects (c); the inner error bars show the statistical component and the outer error bars the total uncertainty.

Figure 7. (a) The measured distribution (dots) of the Ellis-Karliner angle, fully-corrected to the parton level, compared with QCD Monte Carlo calculations. The errors comprise the total statistical and systematic components added in quadrature. The correction factors for detector effects and initial-state radiation (b) and for hadronisation effects (c); the inner error bars show the statistical component and the outer error bars the total uncertainty.

Figure 8. Measured distributions, fully corrected to the parton level (dots), of: (a) scaled energy of the highest-energy jet; (b) scaled energy of the second highest-energy jet; (c) scaled energy of the lowest-energy jet; (d) the Ellis-Karliner angle. The errors

comprise the total statistical and systematic components added in quadrature. The leading-order predictions described in Section 2 are shown as lines: vector (solid), scalar (long dashed), and tensor (short dashed).

Figure 9. Measured distributions (dots) of the event plane orientation angles: (a) $\cos\theta$, (b) $\cos\theta_N$, (c) χ . The errors are statistical only. The predictions of a Monte Carlo simulation are shown as solid histograms.

Figure 10. (a) The measured distribution (dots) of $\cos\theta$, fully-corrected to the parton level, compared with QCD Monte Carlo calculations. The errors comprise the total statistical and systematic components added in quadrature. The correction factors for detector effects and initial-state radiation (b) and for hadronisation effects (c); the inner error bars show the statistical component and the outer error bars the total uncertainty.

Figure 11. (a) The measured distribution (dots) of $\cos\theta_N$, fully-corrected to the parton level, compared with QCD Monte Carlo calculations. The errors comprise the total statistical and systematic components added in quadrature. The correction factors for detector effects and initial-state radiation (b) and for hadronisation effects (c); the inner error bars show the statistical component and the outer error bars the total uncertainty.

Figure 12. (a) The measured distribution (dots) of χ , fully-corrected to the parton level, compared with QCD Monte Carlo calculations. The errors comprise the total statistical and systematic components added in quadrature. The correction factors for detector effects and initial-state radiation (b) and for hadronisation effects (c); the inner error bars show the statistical component and the outer error bars the total uncertainty.

Figure 13. The measured distributions (dots) of $\cos\theta$, fully-corrected to the parton level, in the event thrust ranges: (a) $0.70 < T < 0.80$, (b) $0.80 < T < 0.85$, (c) $0.85 < T < 0.90$, (d) $0.90 < T < 0.95$. The errors comprise the total statistical and systematic components added in quadrature. Fits of Eq. 7 are shown as solid lines.

Figure 14. The measured distributions (dots) of $\cos\theta_N$, fully-corrected to the parton level, in the event thrust ranges: (a) $0.70 < T < 0.80$, (b) $0.80 < T < 0.85$, (c) $0.85 < T < 0.90$, (d) $0.90 < T < 0.95$. The errors comprise the total statistical and systematic components added in quadrature. Fits of Eq. 8 are shown as solid lines.

Figure 15. The measured distributions (dots) of χ , fully-corrected to the parton level, in the event thrust ranges: (a) $0.70 < T < 0.80$, (b) $0.80 < T < 0.85$, (c) $0.85 < T < 0.90$, (d) $0.90 < T < 0.95$. The errors comprise the total statistical and systematic components added in quadrature. Fits of Eq. 9 are shown as solid lines.

Figure 16. Coefficients (a) $\alpha(T)$, (b) $\alpha_N(T)$, (c) $\beta(T)$ from the fits shown in Figs. 13, 14, 15 respectively. Also shown are the leading-order vector (solid), scalar (long dashed)

and tensor (short dashed) gluon predictions.

Figure 17. Leading-order tensor gluon model calculations, based on Eq. 6 (short dashed) and Eq. 18 (dash-dotted), of distributions of: (a) scaled energy of the highest-energy jet; (b) scaled energy of the second highest-energy jet; (c) scaled energy of the lowest-energy jet; (d) the Ellis-Karliner angle.

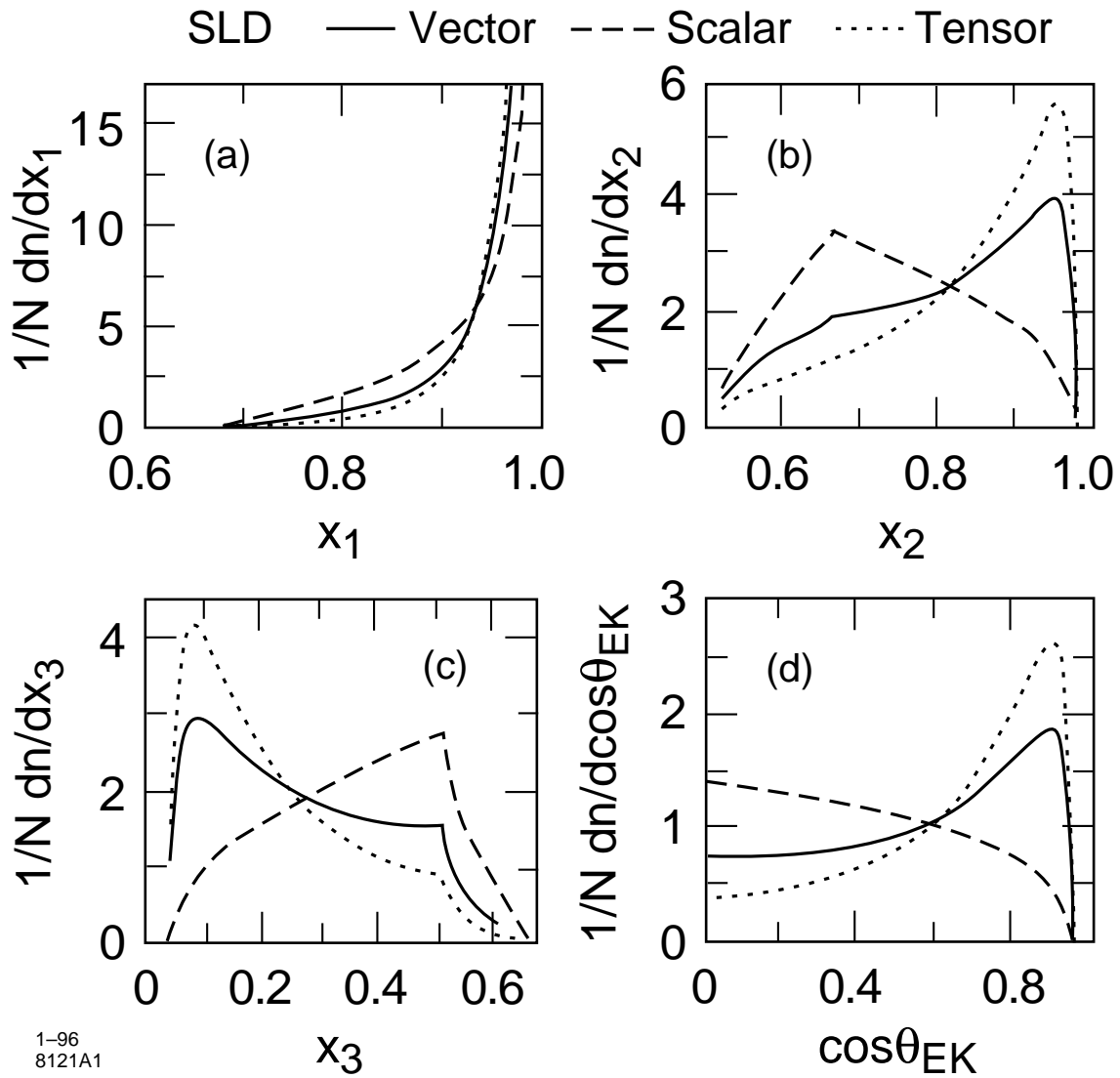
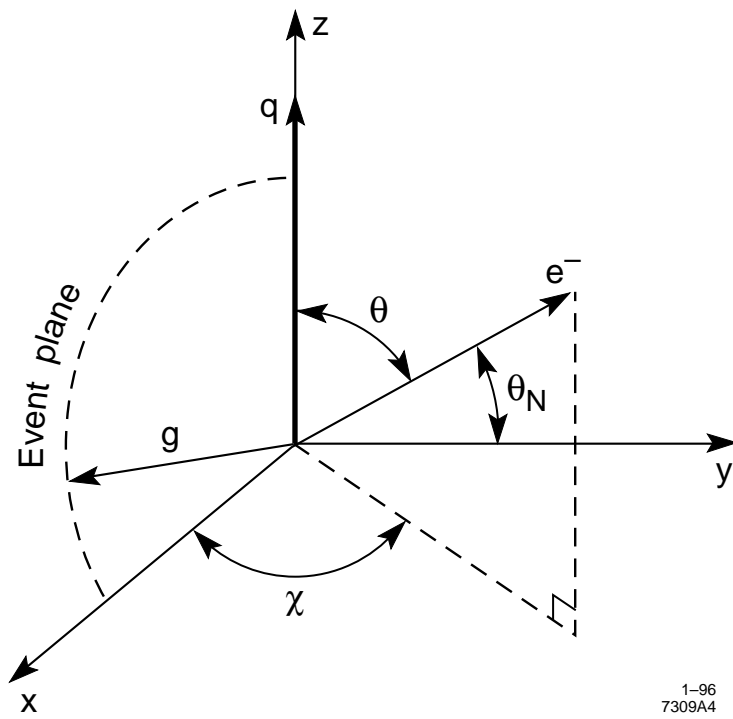


Fig. 1



1-96
7309A4

Fig. 2

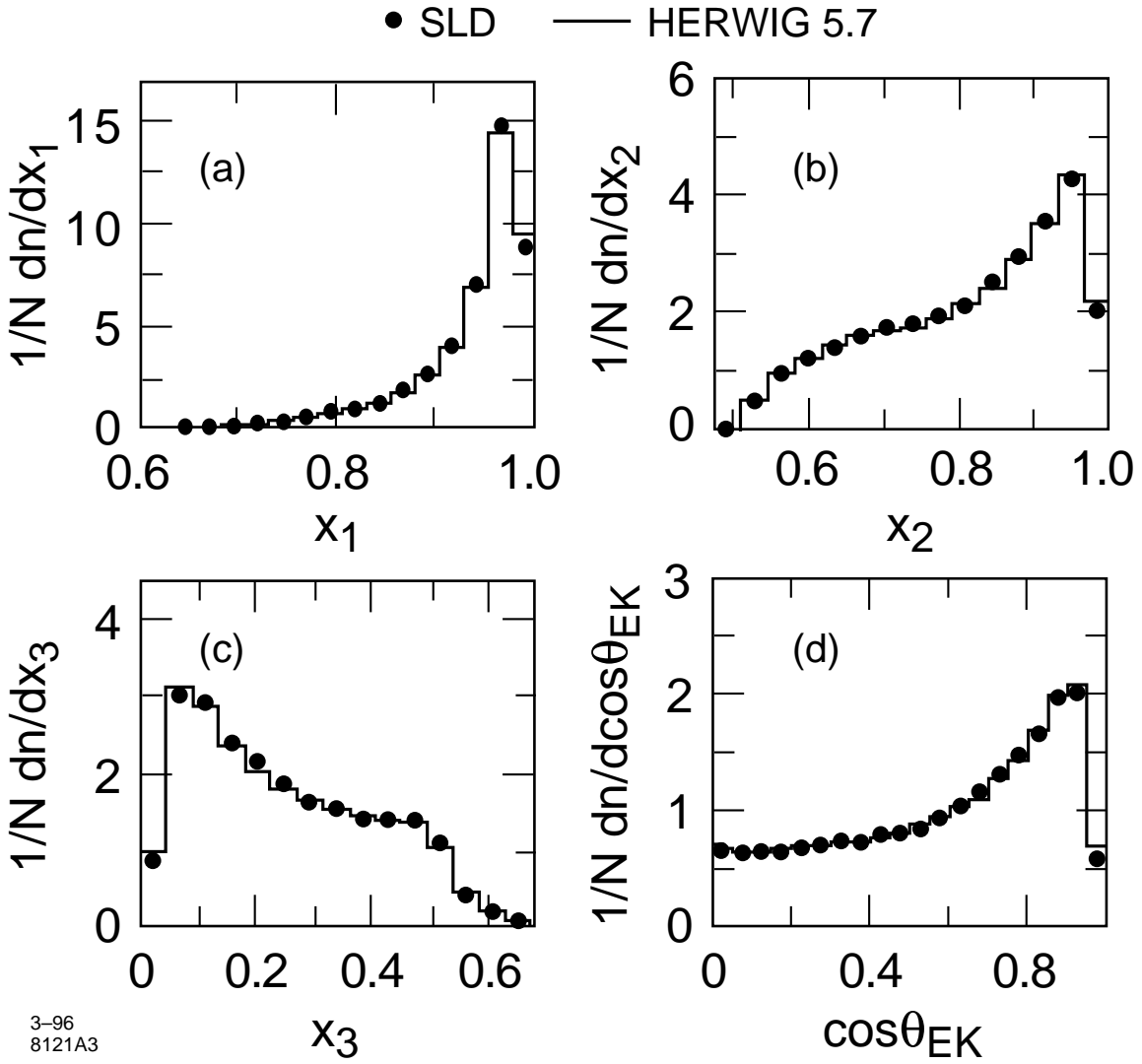


Fig. 3

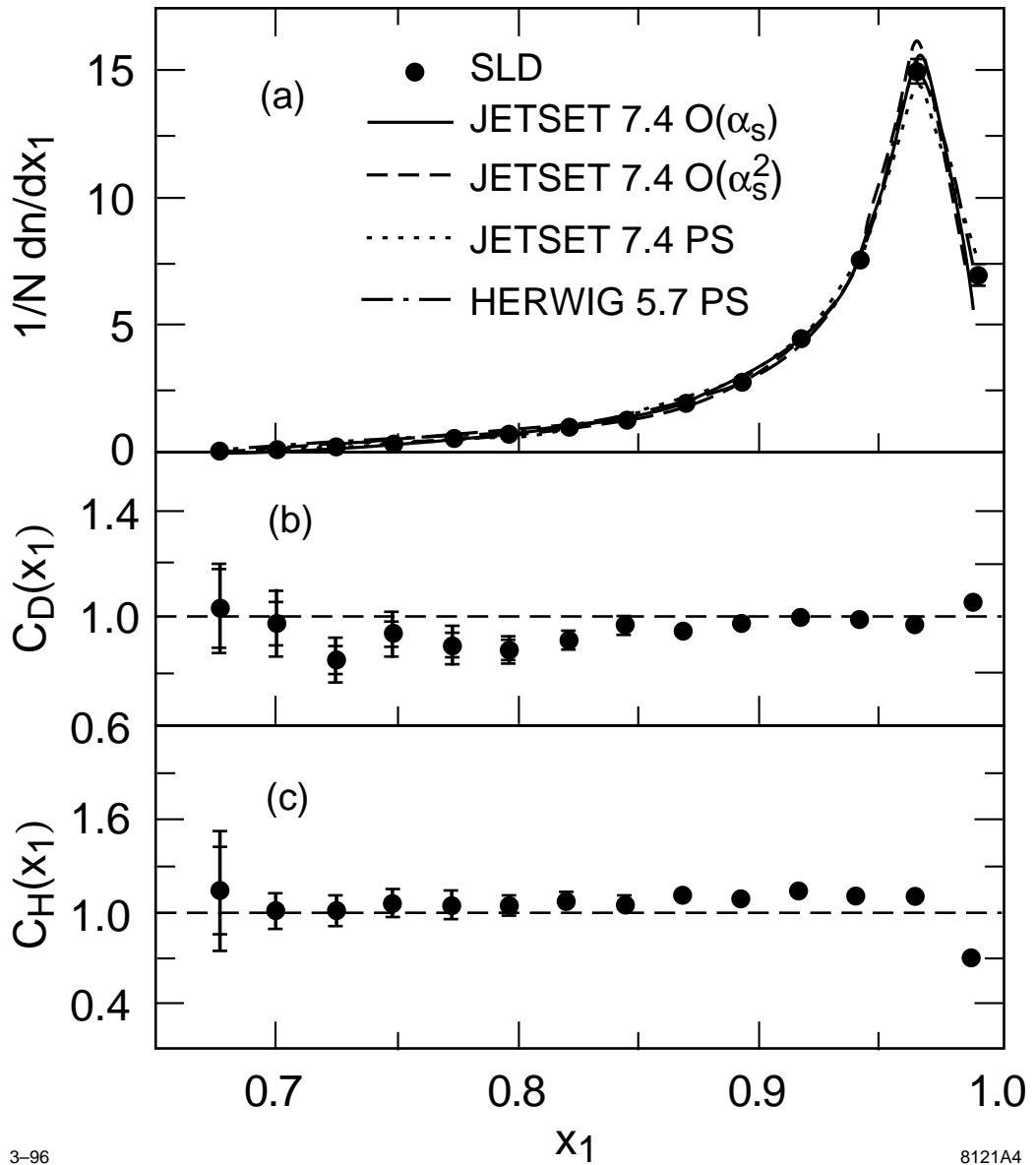


Fig. 4

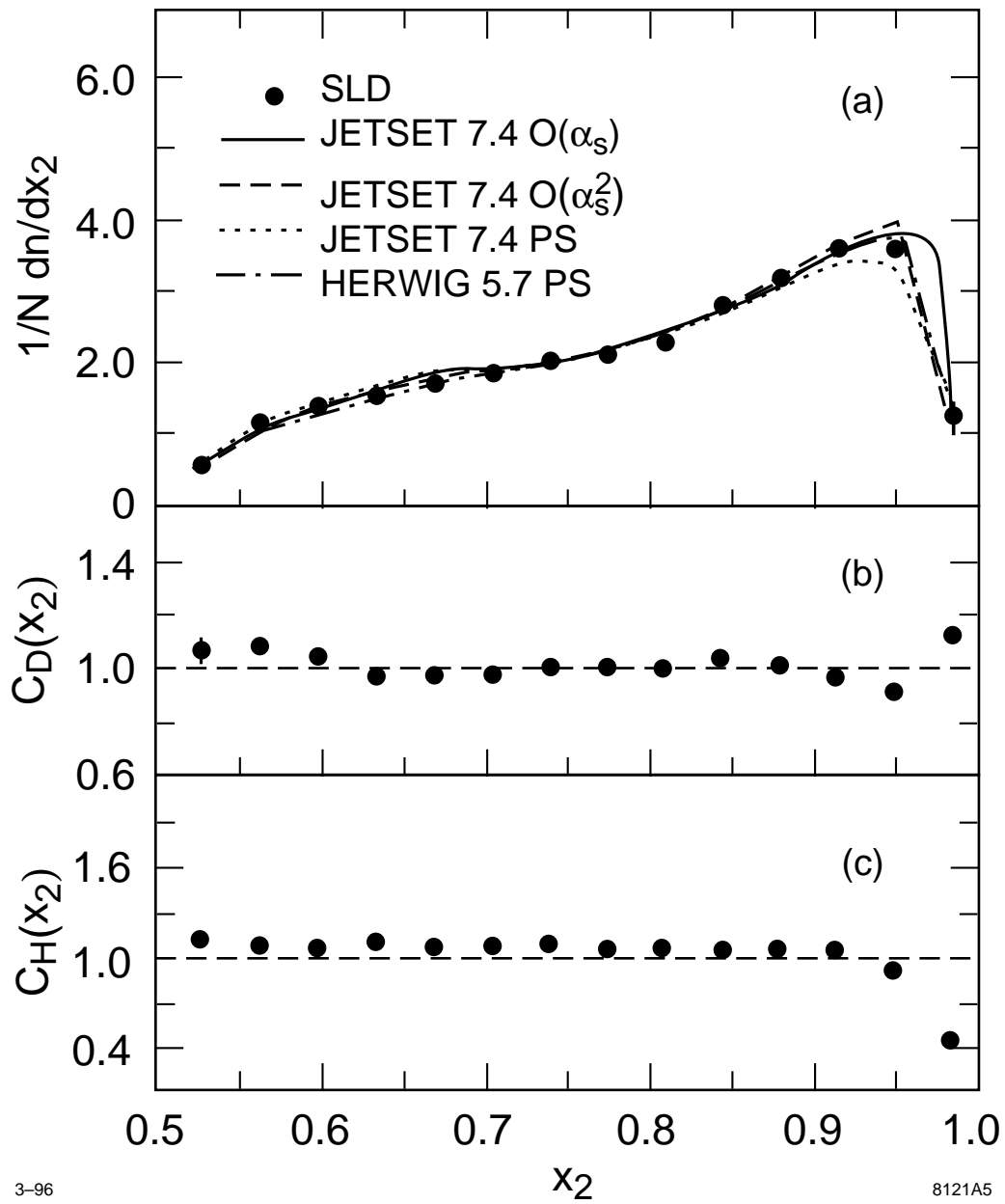


Fig. 5

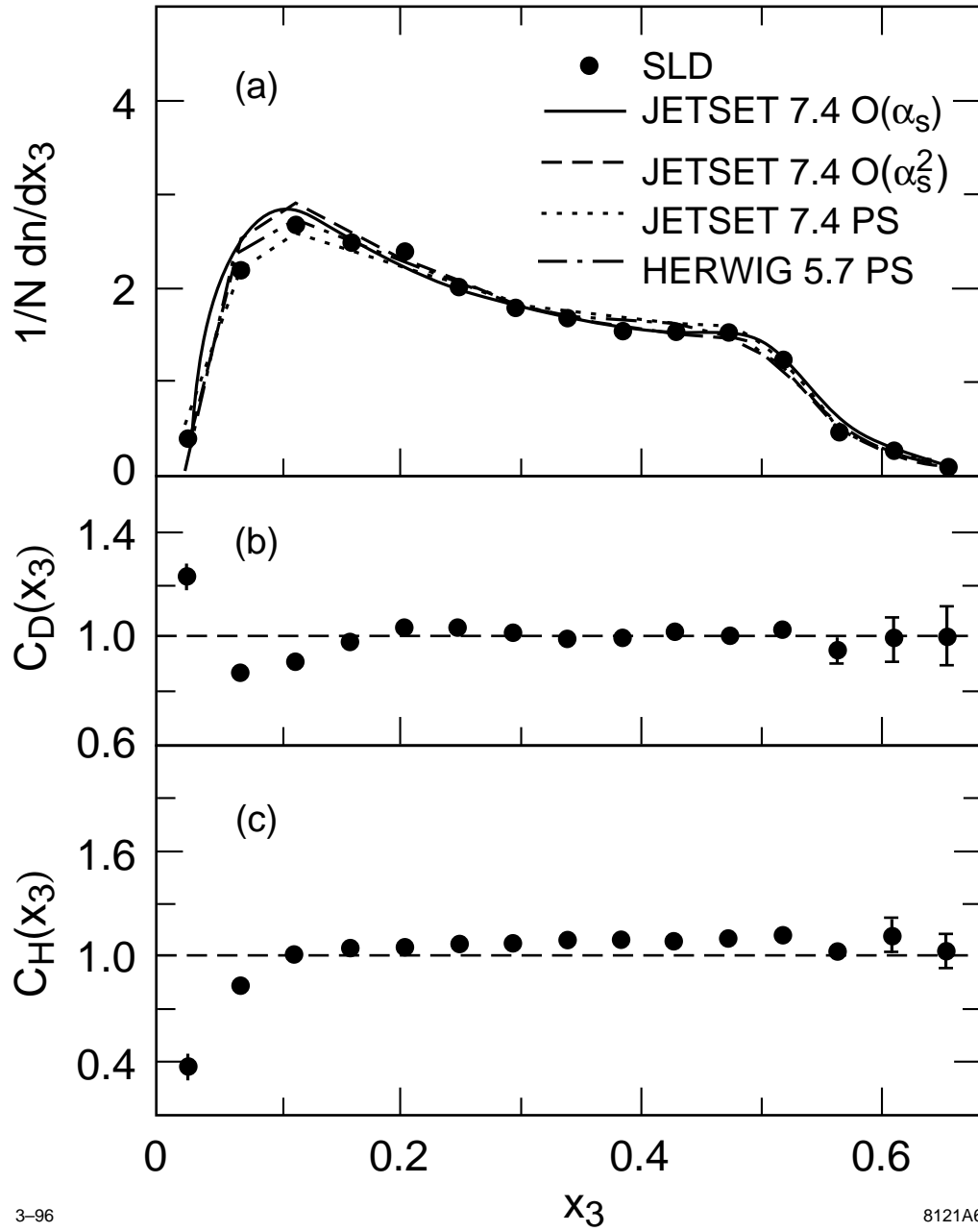


Fig. 6

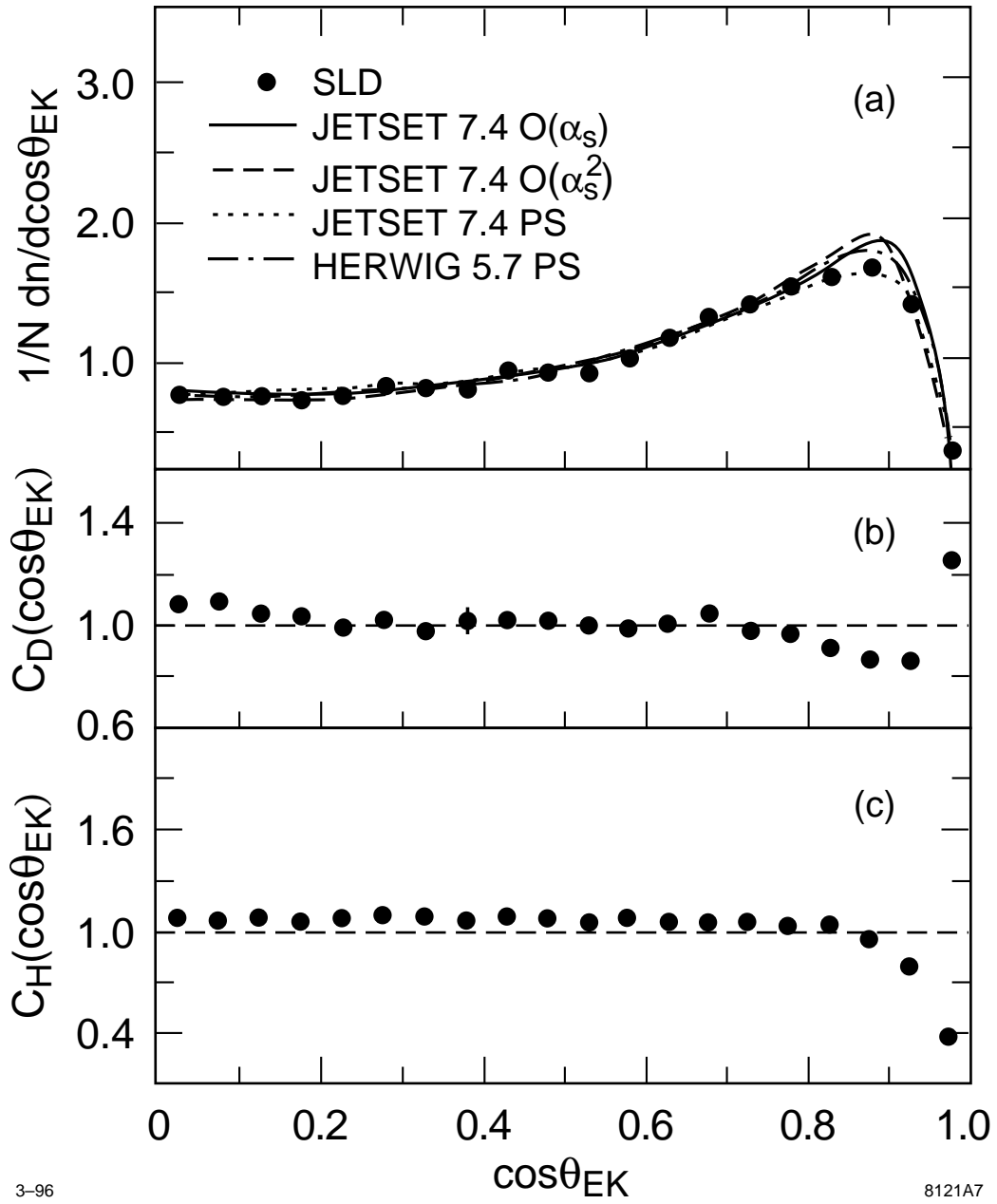


Fig. 7

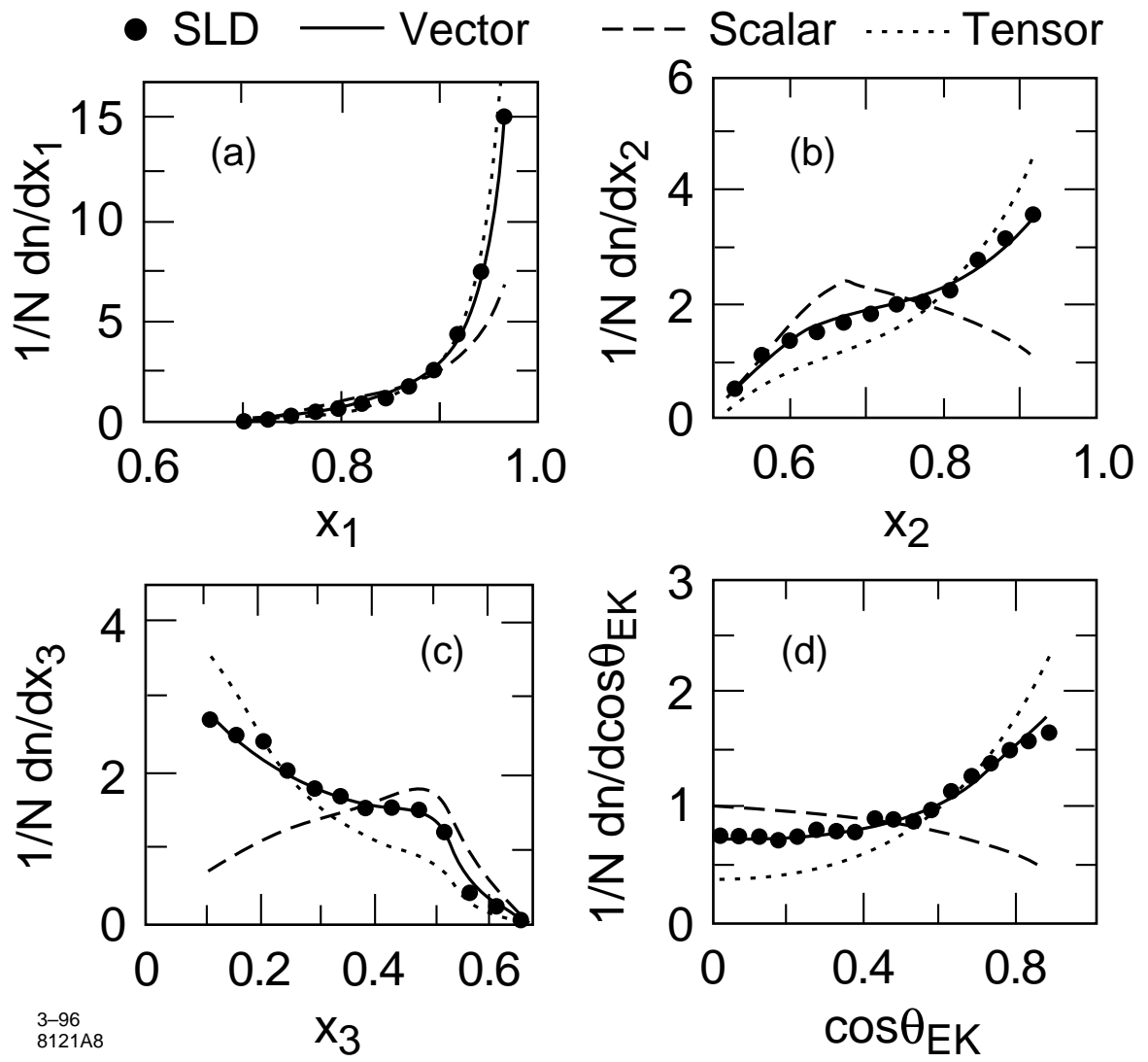


Fig. 8

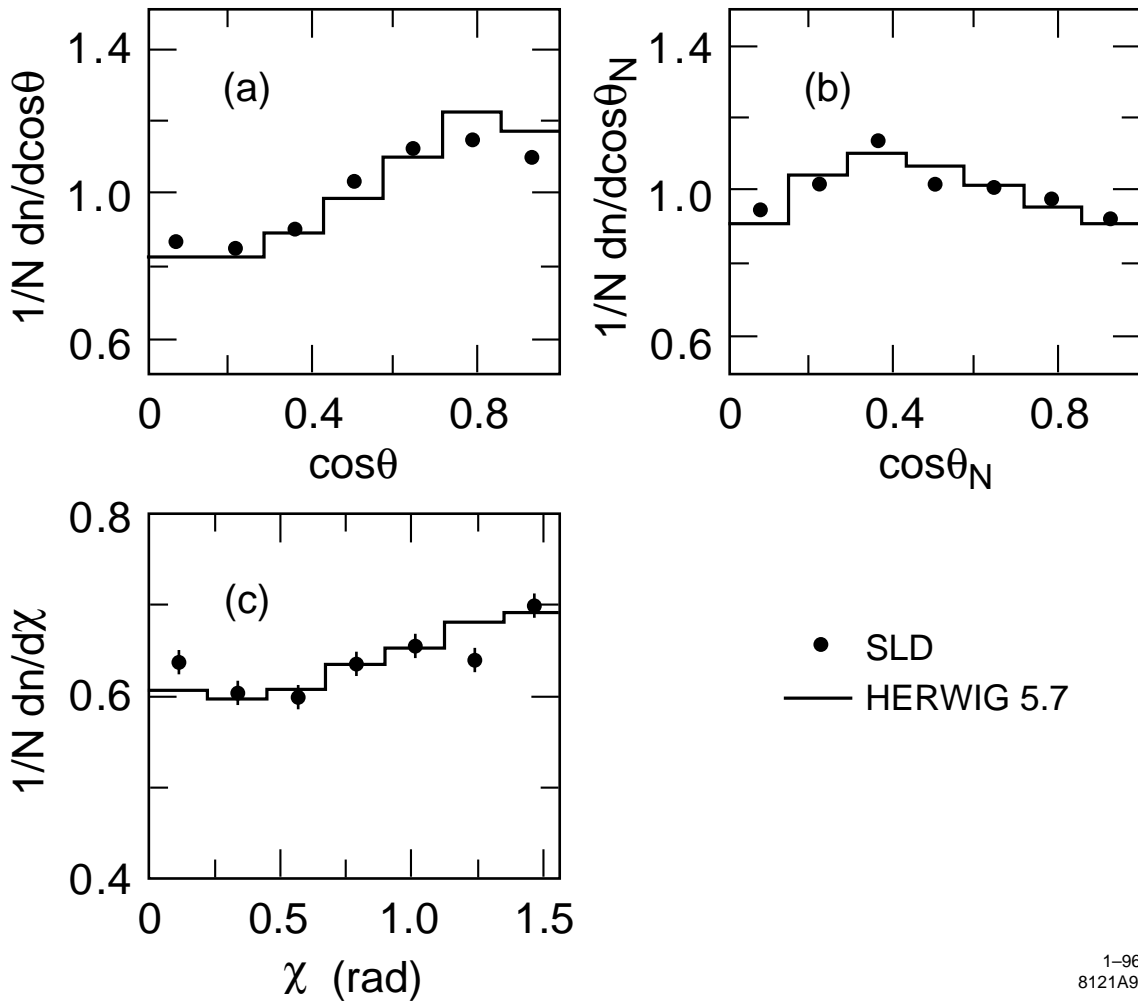


Fig. 9

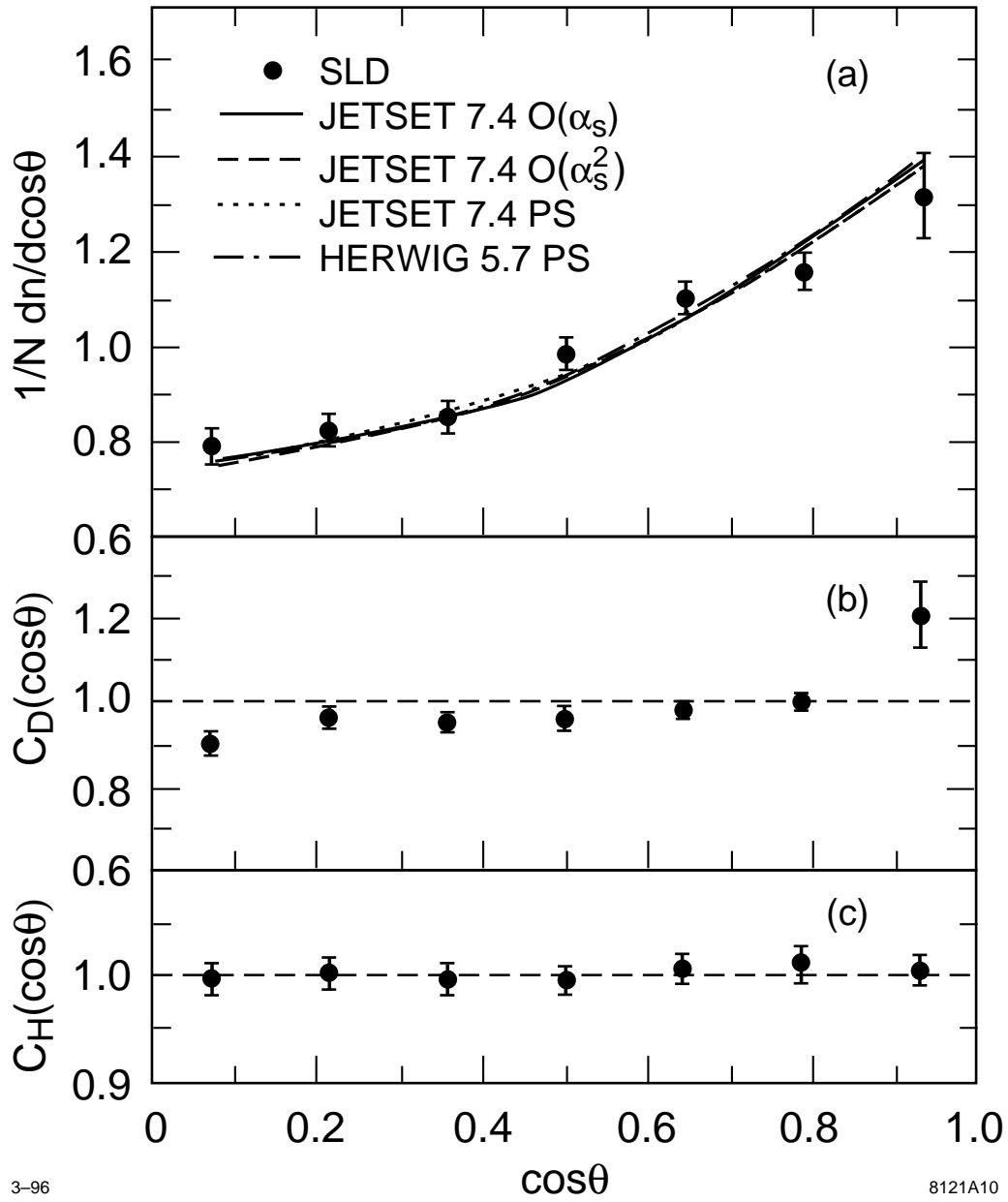


Fig. 10

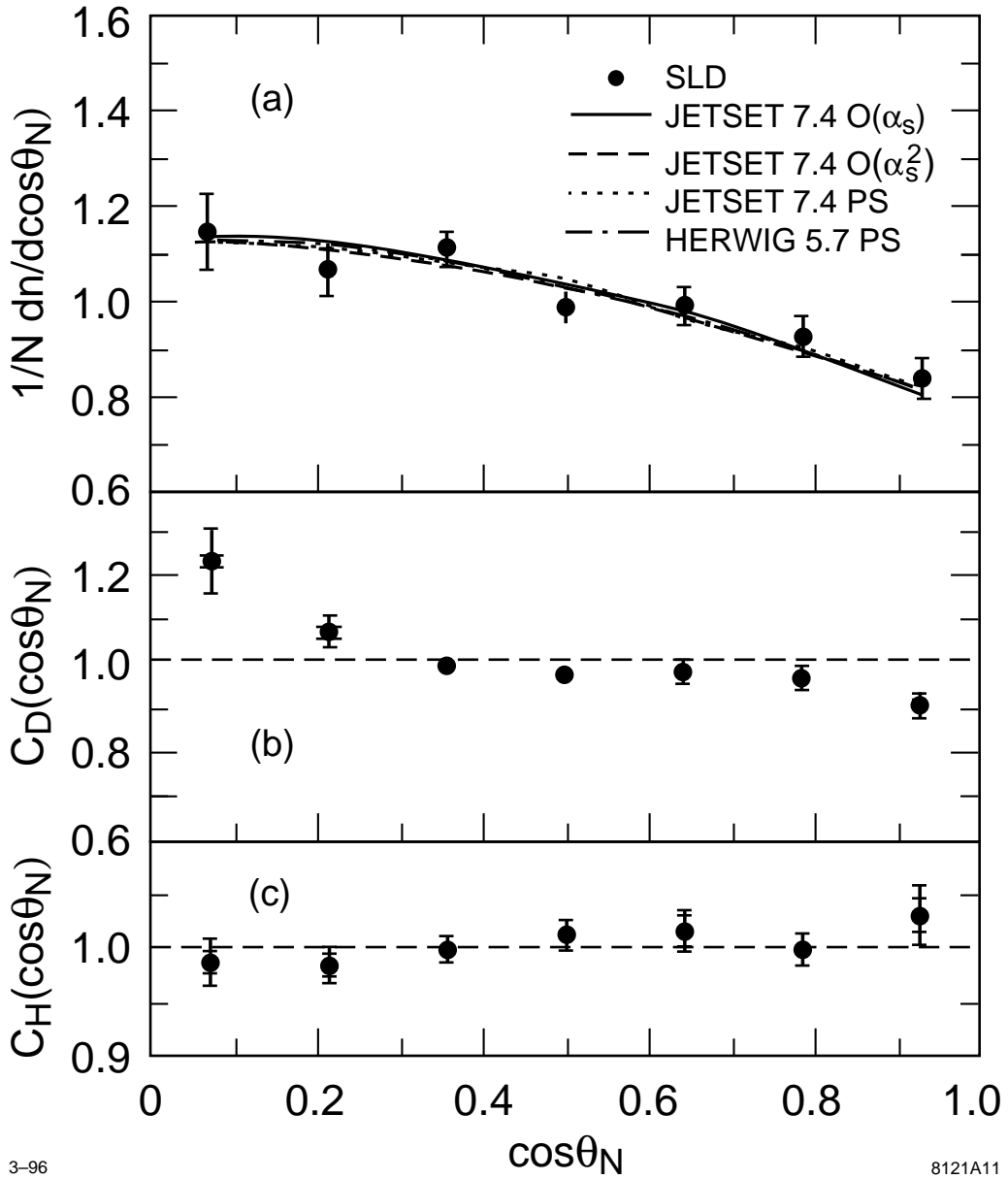


Fig. 11

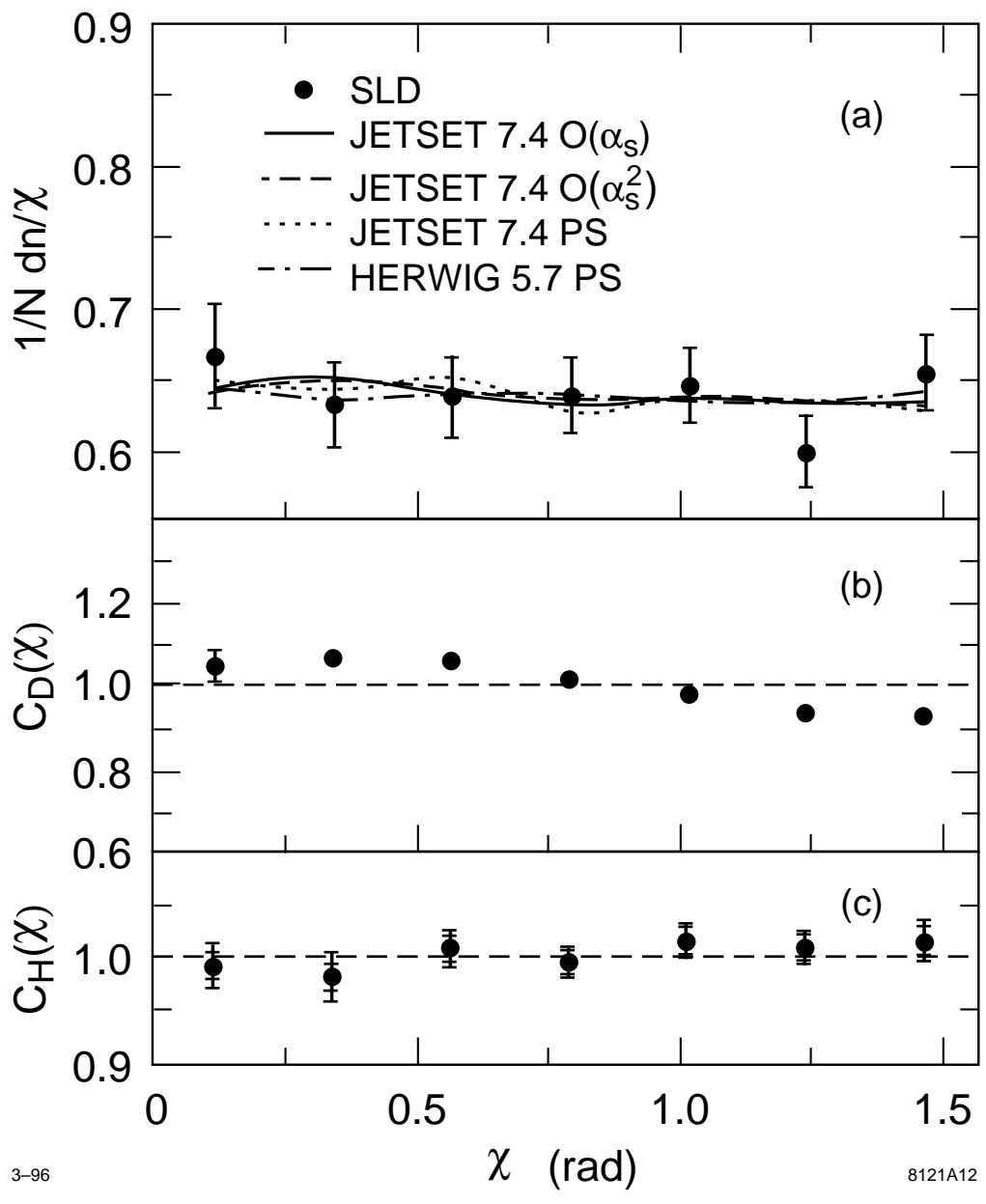
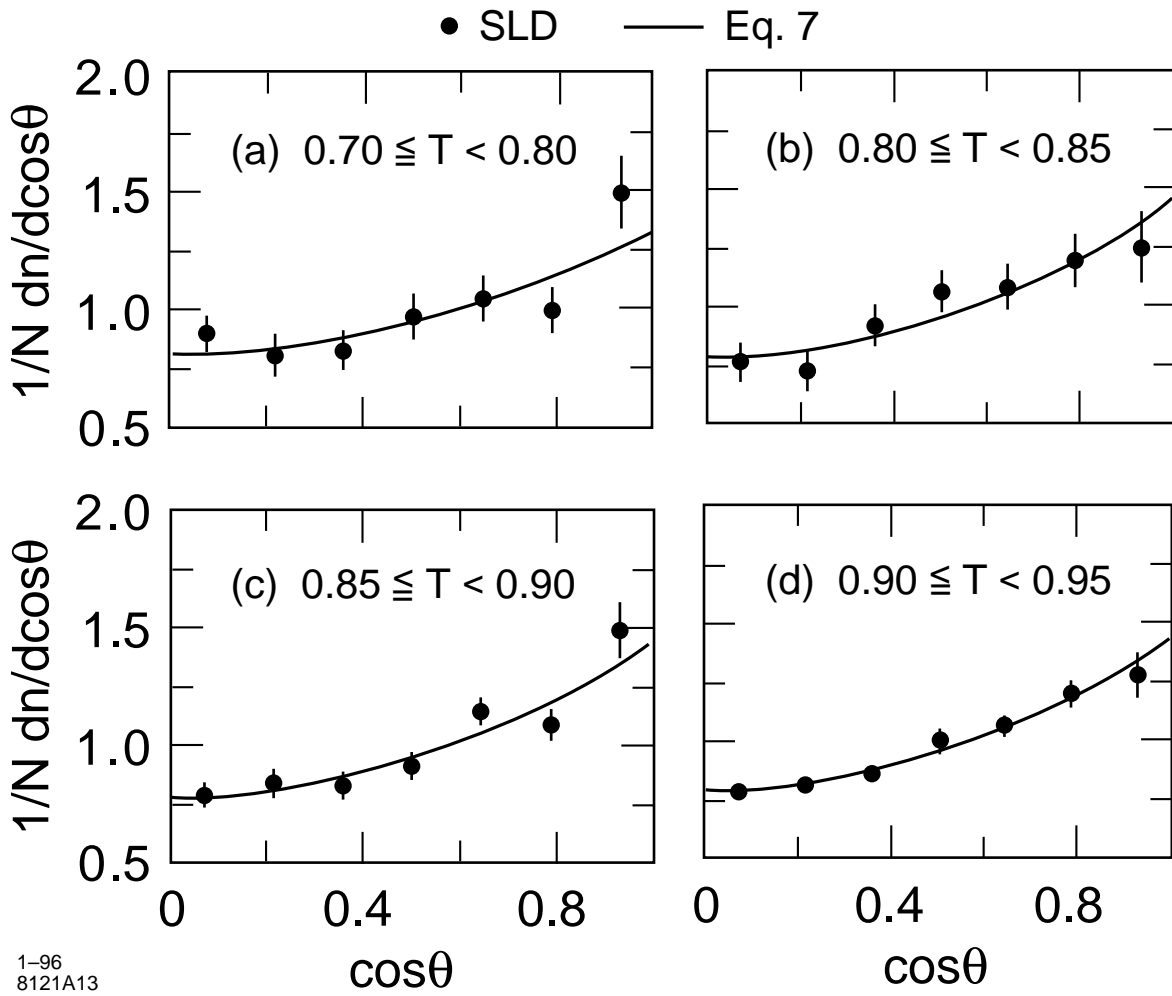
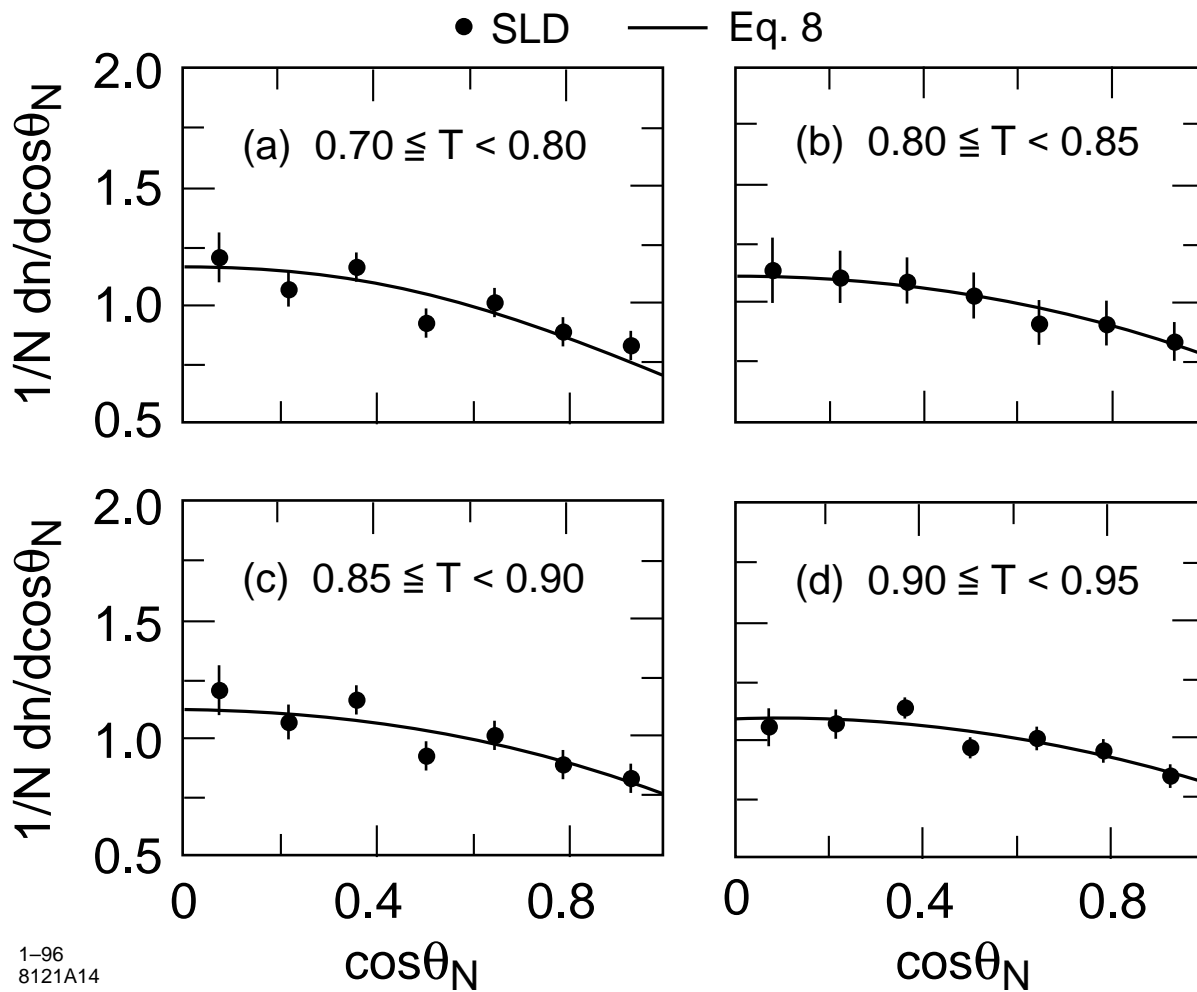


Fig. 12



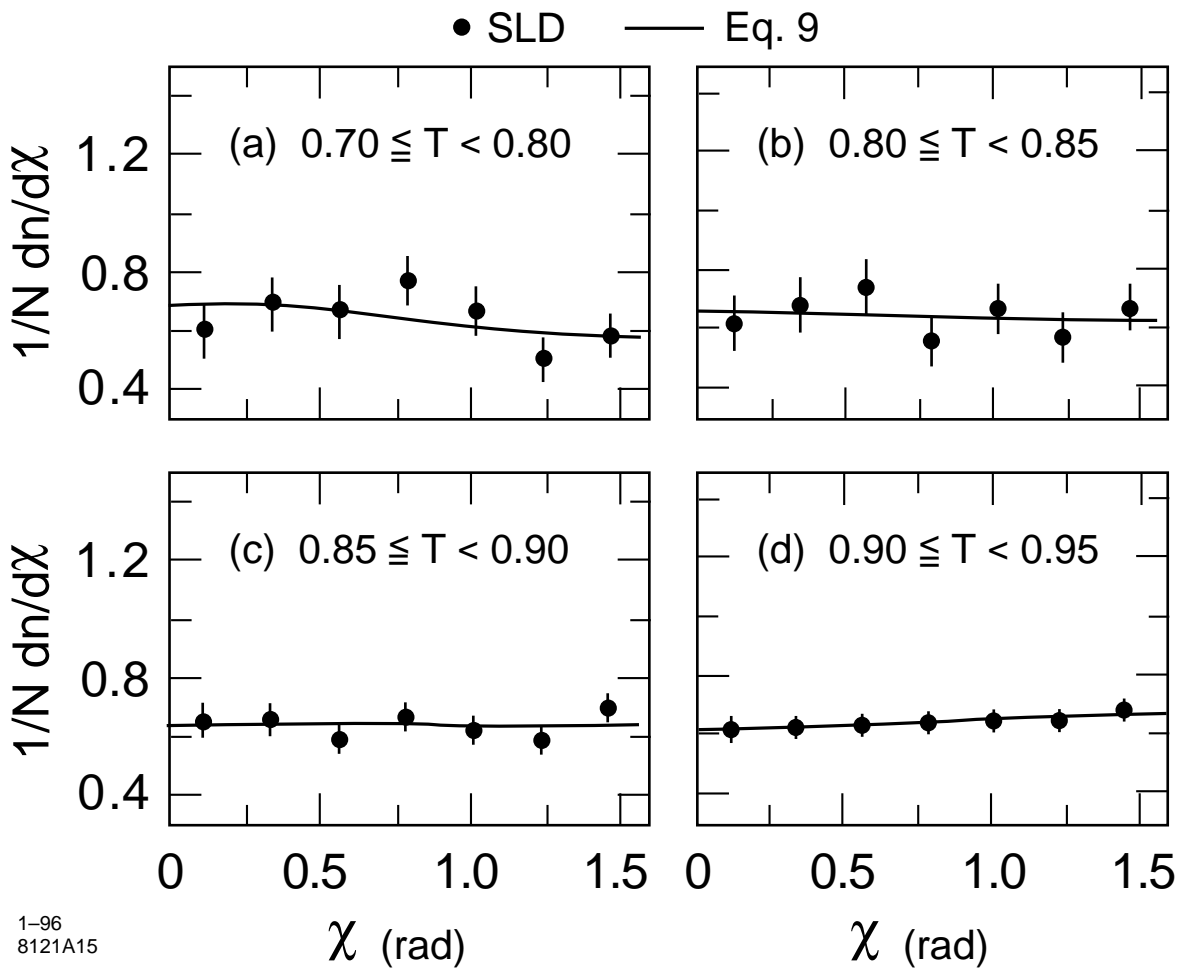
1-96
8121A13

Fig. 13



1-96
8121A14

Fig. 14



1-96
8121A15

Fig. 15

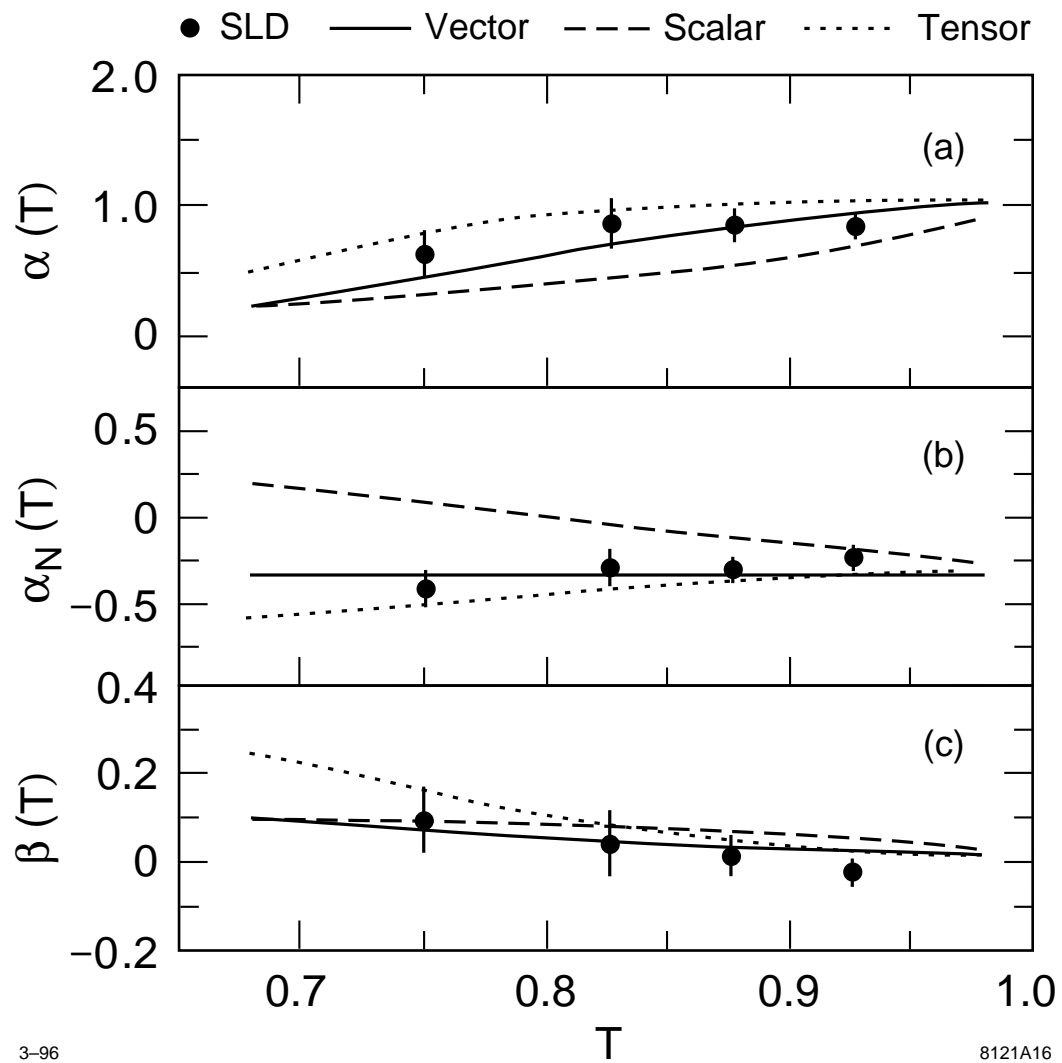


Fig. 16

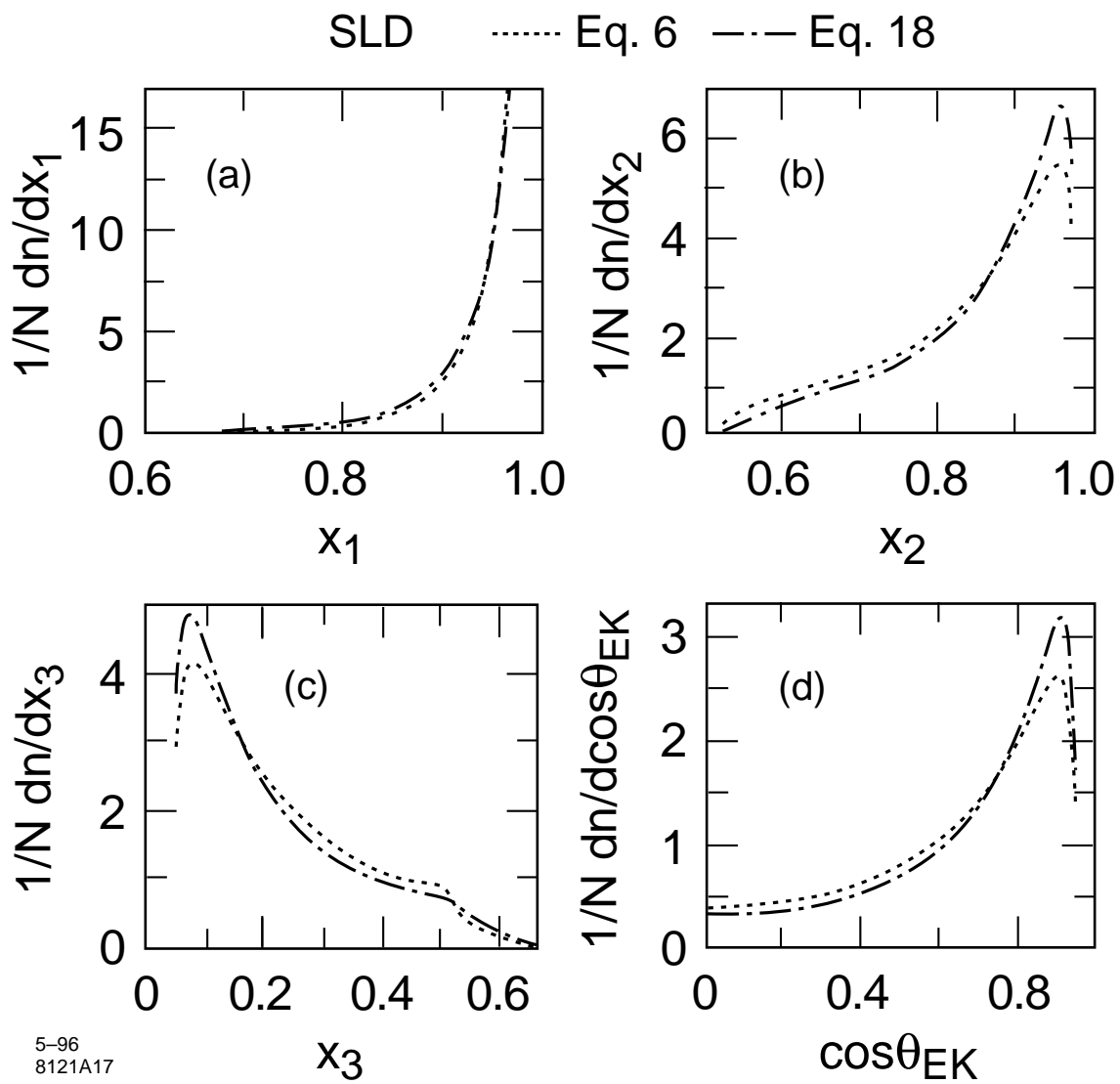


Fig. 17